

Anomalous universal quantum transport in 2D asymptotic quasiperiodic system

Ting-Fung Jeffrey Poon,^{1,2} Yuhao Wan,¹ Yucheng Wang,^{3,4,5,*} and Xiong-Jun Liu^{1,2,4,†}

¹International Center for Quantum Materials, School of Physics, Peking University, Beijing 100871, China

²Hefei National Laboratory, Hefei 230088, China

³Shenzhen Institute for Quantum Science and Engineering,
Southern University of Science and Technology, Shenzhen 518055, China

⁴International Quantum Academy, Shenzhen 518048, China

⁵Guangdong Provincial Key Laboratory of Quantum Science and Engineering,
Southern University of Science and Technology, Shenzhen 518055, China

Quasiperiodic systems extend the concept of the Anderson transition to quasi-random and low-dimensional realms and have garnered widespread attention. Here, we propose the asymptotic quasiperiodic two-dimensional systems characterized by a sequence of rational magnetic fluxes, which have an irrational limit, and predict exotic universal wave-packet dynamics and transport phenomena associated with the asymptotic quasiperiodicity (AQP). The predictions unveil a class of multiple metal-insulator transitions driven by a novel interplay effect between AQP, relaxation, and finite temperature, which further reveals a unified and profound mechanism. Specifically, all the transport phenomena, including the wave-packet dynamics, the bulk and edge transport, are unified in the universal scaling laws unveiled in the asymptotic quasiperiodic regime, which demonstrate a nontrivial asymptotic connection to quantum phases in the quasiperiodic limit. Our work enriches the universal quantum transport phenomena, adds to the basic mechanisms underlying metal-insulator transitions, and opens up an avenue to study the exotic transport physics with AQP in high dimensions.

Introduction.—Quasiperiodic systems [1, 2], positioned between periodic and disordered structures, have garnered widespread attention in recent years, particularly in the context of lower-dimensional Anderson localization [2–27], mobility edges [4–16], multifractal critical phases [17–27], Bose glasses [28–36], and many-body localization [37–44]. Accordingly, quasiperiodic systems show diverse transport phenomena even in one dimension, including localized, subdiffusive, diffusive, superdiffusive, and ballistic transport [45–48]. This contrasts sharply with one-dimensional (1D) disordered systems, which are always localized regardless of disorder strength [49–51]. Similarly, in 2D systems, it is well-established that bulk wave functions become localized with weak disorder [52, 53]. This observation, along with the distinct transport physics in 1D disordered and quasiperiodic systems, prompts one to consider 2D quasiperiodic systems [54–60] to explore unique transport phenomena different from both periodic and random systems.

A most quintessential 2D phenomenon is the integer quantum Hall effect observed in electronic gases subjected to strong perpendicular magnetic fields, where the Hall conductivity is quantized to integer (Chern number) multiples of e^2/h , with vanishing longitudinal conductivity, revealing its topological properties [61]. The 2D quasiperiodic Hall systems are obtained when the magnetic flux $2\pi\phi$ per unit cell is irrational. In addition to synthetic quantum systems like optical lattices, in which the synthetic magnetic fluxes can be generated through light-atom couplings, recently the 2D twisted Moiré materials show also feasibility in tuning the flux ϕ due to much enlarged unit cells and attracted considerable interests [62–66]. In the real experiment, an exact irrational flux is hard to engineer. For a rational magnetic flux $\phi = p/q$, the system is effectively quasiperiodic when the magnetic unit cell, determined by q , is larger than system size, but it is always periodic in the thermodynamic limit. An intriguing open

issue is that, whether the transport physics in 2D system with irrational magnetic flux can be studied and probed from that in systems with rational flux in the thermodynamic limit?

In this Letter, we propose the 2D asymptotic quasiperiodic Hall systems, which are characterized by a rational sequence of magnetic fluxes $\phi_n = p_n/q_n$, with only the limit ϕ_∞ being irrational, and predict the interplay effects of the asymptotic quasiperiodicity (AQP), relaxation, and temperature, which lead to unprecedented multiple anisotropic metal insulator transitions (MITs). The qualitatively nontrivial transport phenomena with rational ϕ_n , including wave packet dynamics, bulk and edge transport, are observed and have a unified profound mechanism interpreted as universal scaling laws, which are deeply connected to the quantum phases in the quasiperiodic limit characterized by ϕ_∞ . The predicted new multiple MITs are different from those driven by the celebrated mechanisms [67, 68], including by spontaneous symmetry breaking [69–72], Lifshitz transition [73, 74], Mott gap in Hubbard models [75], and by the (quasi-)disorders [52, 76, 77]. These results highlight the exotic universal transport physics in the asymptotically quasiperiodic 2D systems, and can be applied to the recently attractive 2D Moiré materials.

Model.—We start with a 2D square lattice model with an asymptotically incommensurate magnetic flux $2\pi\phi$ threading each plaquette. By taking the gauge $\mathbf{A} = A_d \hat{e}_d$ with $A_d = 2\pi\phi j_{\bar{d}}$, the Hamiltonian can be written as

$$H = \sum_{j\bar{d}} t_d e^{-2\pi i \phi j_{\bar{d}}} c_{j_{\bar{d}}+1, j_{\bar{d}}}^\dagger c_{j_{\bar{d}}} + t_{\bar{d}} c_{j_{\bar{d}}, j_{\bar{d}}+1}^\dagger c_{j_{\bar{d}}} + h.c., \quad (1)$$

where d represents the x or y direction, $\bar{d} \perp d$, t_d is the hopping along d -direction, and $\phi = \phi_n = p_n/q_n$ is rational, except for the finite irrational limit ϕ_∞ . For example, $\phi_\infty = (\sqrt{5} - 1)/2$ can be approximated via Fibonacci sequences [78]. After performing Fourier transformation along

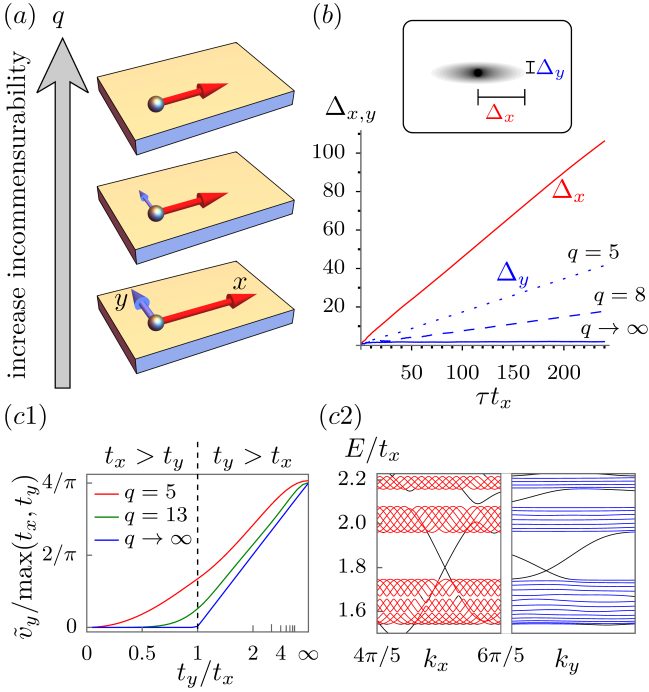


Figure 1. (a) Schematic diagram showing how AQP impacts transport behavior for $t_x > t_y$. As q increases, the system becomes more localized (denoting by shorter arrowed lines) in the y -direction, while remaining at a nonzero value along x even as $q \rightarrow \infty$. (b) $\Delta_{x,y}$ vs time. $\phi = 3/5, 5/8$ and $(\sqrt{5}-1)/2$ for the dotted, dashed and solid blue lines, respectively. (c1) \tilde{v}_y vs hopping. $\phi = 3/5(8/13)$ for the red (green) line. The blue line represents both $\phi = 144/233$ and $q \rightarrow \infty$ that overlaps. (c2) The zoomed-in band structure vs k_x (red) and k_y (blue) for $\phi = (\sqrt{5}-1)/2$. $t_x = 1$ and $t_y = 0.7$ for (b,c2). The black lines represent the edge states at the gap.

d -direction, we have $H = \sum_{k_d} H_{1D}(k_d)$, where $H_{1D}(k_d) = \sum_{j_{\bar{d}}} 2t_d \cos(2\pi\phi j_{\bar{d}} + k_d) c_{k_d j_{\bar{d}}}^\dagger c_{k_d j_{\bar{d}}} + t_{\bar{d}} (c_{k_d, j_{\bar{d}}+1}^\dagger c_{k_d j_{\bar{d}}}) + h.c.$ gives the Aubry-André-Harper model for irrational $\phi = \phi_\infty$ [2]. Then, for $t_d > t_{\bar{d}}$ the system is localized (extended) along the \bar{d} -direction (d -direction) [79]. Note that if we rewrite Eq. (1) in the $A_{\bar{d}}$ gauge, the system is translational invariant in \bar{d} direction. As gauge transformation does not change physics, this leads to a puzzle: why the states are localized in the translational invariant \bar{d} -direction? We shall resolve this puzzle below by revealing a novel mechanism for Anderson localization in this 2D system. More importantly, instead of focusing on the quasiperiodic limit $\phi = \phi_\infty$, here we consider AQP regime with fluxes varying according to the rational sequence $\phi_n = p_n/q_n$ [Fig. 1(a)], and explore the new universal transport physics regarding the sequence, beyond the extended and localization phases.

Bulk transport.—We first consider the coherent wavepacket dynamics. Let the wavepacket $\psi(0)$ be initially centered at (x_0, y_0) , and we examine the directional mean-square displacement at time τ defined by $\Delta_d(\tau) = \sqrt{\langle (d-d_0)^2 \rangle_{\psi(\tau)}}$ for the wavefunction $\psi(\tau) = e^{-iH_y\tau}\psi(0)$. Then for $t_x > t_y$

we have the generic relation ($q = q_n$)

$$\Delta_x = C_1\tau; \Delta_y = \begin{cases} C_2\tau, & \text{for rational } \phi = \frac{p}{q} \\ \tilde{C}_3, & \text{for irrational } \phi \end{cases} \quad (2)$$

where the constants $C_{1,2}$ depends on q . We set $\psi(0) = \mathcal{N}e^{-((j_x-x_0)^2+(j_y-y_0)^2)/\Delta_0}$, with Δ_0 being initial wavepacket width, and simulate the average over x_0 and y_0 , and find that the coefficients exhibit distinct universal scalings

$$\langle C_2 \rangle \sim \tilde{C}_2 t_x (t_y/t_x)^q, \langle C_1 \rangle \sim \tilde{C}_1 (t_x - t_y) + q^{-1} \tilde{C}_4 \sqrt{t_x t_y} \quad (3)$$

with $\tilde{C}_{1,2,3,4}$ being of order 1 [80] and $\langle \cdot \rangle$ denoting the average of p and $\psi(0)$. The displacement speed $\langle C_2 \rangle$ exhibits a clear exponential law versus q . This is because the ballistic transport along y direction can be reached only after every q -site hopping, corresponding to the q -th order perturbation process. In contrast, $\langle C_1 \rangle$ consists of two terms, one independent of q and the other having a power-law relationship with q (details in supplementary material [80]). The distinct scaling laws in the ballistic transport in two directions for finite q show non-trivial connection to the localization (extended) phase in the $y(x)$ -direction in the incommensurate limit $q \rightarrow \infty$ [Figs. 1(a,b)]. We then examine the maximal group velocity in the y -direction and averaged over all bands. After some algebra we can obtain that [Fig. 1(c1)] [80]

$$\tilde{v}_y \sim \begin{cases} t_x (t_y/t_x)^{q/2}, & \text{for } t_x > t_y, \\ \frac{4}{\pi} (t_y - t_x) + \tilde{C}_5 q^{-1} \sqrt{t_x t_y}, & \text{for } t_x < t_y, \end{cases} \quad (4)$$

with \tilde{C}_5 being of order 1. The scaling exponent for $t_x > t_y$ is $q/2$ rather than q . This is understood in the following way. We transform the Hamiltonian in A_y gauge to k -space in both directions, yielding $H = \sum_{k_x, k_y} 2t_x \cos(k_x) c_{k_x k_y}^\dagger c_{k_x k_y} + (t_y e^{ik_y} c_{k_x+2\pi\phi, k_y}^\dagger c_{k_x, k_y} + h.c.)$. Then \tilde{v}_y is proportional to maximum bandwidth of subbands versus k_y , parameterized by k_x . The original band splits into q subbands due to the transitions between states with k_x and $k_x + 2\pi\phi$. For this the q states with diagonal potentials $2t_x \cos k_x$ ($\tilde{k}_x = k_x, k_x + 2\pi\phi, \dots, k_x + 2\pi(q-1)\phi$) are coupled together. The bandwidths determined by the maximum transitions are obtained from the set of q states with $k_x = 0$, which separate into two equal groups, with each including $q/2$ distinct potentials. Thus the $q/2$ -th order perturbation [$\sim (t_y/t_x)^{q/2}$] determines the bandwidth and maximal group velocity [80].

With Eqs. (2-4) we reach a new mechanism for the Anderson localization in y direction, which is translational invariant under A_y gauge, in the case of $t_x > t_y$ and $\phi = \phi_\infty$. In Fig. 1(c2) we plot the energy dispersion versus k_x and k_y , in A_x and A_y gauges, respectively. In contrast to the dispersive bands with k_x , all the bulk subbands become flat versus k_y , consistent with the fact that \tilde{v}_y exponentially decays to zero with increasing q and $\tilde{v}_y(q \rightarrow \infty) = 0$. This shows a novel mechanism that Anderson localization in the Aubry-André model (in A_x gauge) is equivalently mapped to 1D Bloch flat bands (in A_y gauge) through gauge transformation.

We then investigate the universal bulk transport phenomena in the presence of relaxation at zero temperature. The DC longitudinal conductivity with relaxation is written as

$$\sigma_{dd} = \frac{e^2}{h} \int \frac{d^2k}{(2\pi)^2} \Re \left\{ \text{tr} \left[(G_0^+ - G_0^-) \frac{d\mathcal{H}}{dk_d} G_0^- \frac{d\mathcal{H}}{dk_d} \right] \right\}, \quad (5)$$

where $\Re\{\cdot\}$ denotes the real part, $G_0^\pm = (E_F \pm i\Gamma - \mathcal{H})^{-1}$, \mathcal{H} is Fourier transformation of H into 2D k -space, and Γ denotes a finite relaxation rate, which originates from a uniform spatial decay effect [80–83], such as the coupling of a 2D material to a substrate [84, 85] or the introduction of losses at each site in cold atom systems [86, 87]. Examination on σ_{yy} reveals that there are three qualitatively different regions [Fig. 2] [80]: (A) Metal I. $\sigma_{yy} \propto \Gamma^{-2}$ in the region with sufficiently large $\Gamma > \Gamma_{c1}$; (B) Metal II. $\sigma_{yy} \propto \Gamma^{-1}$ in the region with sufficiently small $\Gamma < \Gamma_{c2}$; (C) Insulator. $\sigma_{yy} \propto \Gamma^\alpha$, where $\alpha \approx 1$ at the intermediate region. The scalings of σ_{yy} in regions A and B can be proven by asymptotic behaviors of Eq. (5). For large Γ , $\sigma_{yy} = e^2(2h\Gamma^2\pi^2)^{-1} \int dk_x dk_y \text{tr} [\mathcal{H}^2]$; for small Γ , $\sigma_{yy} = e^2(4h\Gamma\pi^2)^{-1} \int dk_x dk_y \sum_b \delta(\epsilon_b(k_x, k_y) - \mu)(\partial\epsilon_b/\partial k_\alpha)^2$, where ϵ_b is the energy of the b -th band. The critical relaxation rates $\Gamma_{c1, c2}$ satisfy the scalings [80]

$$\Gamma_{c1} \sim t_y; \Gamma_{c2} \sim t_x(t_y/t_x)^q, \quad (6)$$

which are universal and have profound mechanism. Note that $1/\Gamma$ denotes a time scale, during which each particle is scattered once. The flux ϕ splits the original Bloch band into q magnetic bands, which dominate the ballistic bulk transport in the weak relaxation limit, giving a band metal phase (Metal II), in which $\sigma_{yy} \propto \Gamma^{-1}$, similar to Drude model. In the opposite strong Γ limit, the phase information associated with magnetic flux is wiped out, so the band splitting between the magnetic bands is removed. Then the ballistic transport is dominated by the original Bloch band results, rendering the Metal I region. In this region, the conductivity is $\sigma_{yy} \propto \Gamma^{-2}$, which arises from both the dephasing and decay of particles in the case of strong relaxation (each effect contributes to a factor Γ^{-1} of σ_{yy}). The most nontrivial region is in-between, in which the relaxation and AQP effect compete, rendering the mechanism of the universal scalings at the critical transitions. The particles see the magnetic unit cell only after it can coherently hop q sites without being fully scattered since the magnetic unit cell is expanded by q times. This leads to a critical relaxation rate Γ_{c2} proportional to q -th order of the hopping couplings, i.e. $\sim (t_y/t_x)^q$, beyond which the coherent hopping of particles is limited within a unit cell, and then they experience an effective quasiperiodic system, instead of periodic system with magnetic bands, giving the intermediate insulating phase. We see that Γ_{c2} decays exponentially with q , so a tiny Γ drives the periodic Hall system to be effectively quasiperiodic at relatively large q . In the incommensurate limit $q \rightarrow \infty$, the Metal-II phase disappears and σ_{yy} vanishes for $\Gamma \rightarrow 0$, but is finite for $\Gamma > 0$. Furthermore, if the particles are fully scattered within every single hopping process (with time scale $1/t_y$), the effective quasiperiodicity is fur-

ther removed, giving the other critical point $\Gamma_{c1} \sim t_y$. In the $\Gamma > \Gamma_{c1}$ regime, the bulk reenters metallic phase generically, even E_F is in the band gap [insert of Fig. 2]. Finally, in the Supplementary Material [80], we also show that the insulating region turns to a critical metal phase with $\sigma_{yy} = \sigma_{xx} \sim \Gamma^{-1/2}$ in the isotropic regime $t_x = t_y$. To observe these results in real experiment requires that the system size be large compared to the size (q) of a unit cell.

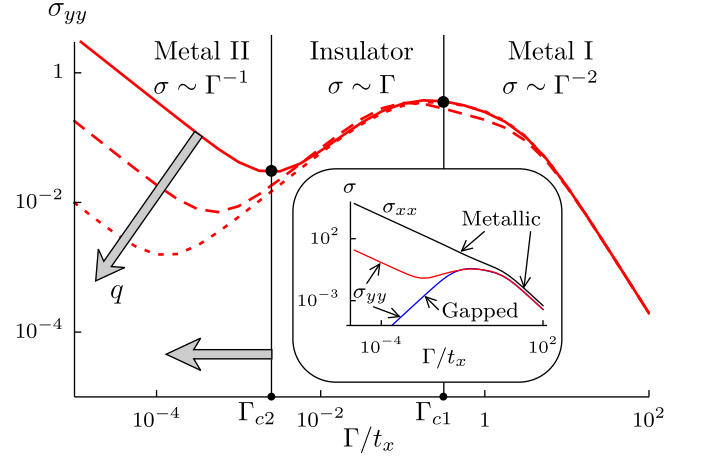


Figure 2. σ_{yy} vs Γ , where $t_x = 1, t_y = 0.7$. $\phi = 8/13, 11/17$, and $13/21$ for the solid, dashed and dotted red lines, respectively. The two gray arrows in the Metal II region indicate that as q increases, Γ_{c2} approaches 0 exponentially. Inset: Black: σ_{xx} . Red (Blue): Typical σ_{yy} if E_F is at the band (inside gap for QHE regime).

Edge transport.—Now we turn to quantum transport contributed by edge states in a finite size system. The localization length ξ_d , characterizing the spatial distribution of the edge states along d -direction, may be dominated by two different aspects – the topological gap E_g or the quasiperiodicity. Similarly, we consider $t_x > t_y$. The edge states at x -boundary exhibit conventional behavior with $\xi_x \propto E_g^{-1}$, as the system is extended in the x -direction [Figs. 3(a,b)]. The localization length ξ_y of edge states in the y -boundary may be dominated by the bulk gap E_g or the AQP quantified by q . In most cases that E_g is small ($E_g \ll q^{-1}t_x$), the universal scaling with exponential decay of the bulk versus q in the y -direction determines that $\xi_y \propto q$, and we analytically find [80]

$$\xi_y = \left(-\log \frac{t_y}{t_x} + 2q^{-1} \log 2 \right)^{-1}, \quad (7)$$

which is independent of E_g , as shown in Fig. 3(b). If we consider one direction having periodic boundary condition and another being open, the critical system size, beyond which the edge states in x (or y)-boundary are decoupled, is $L_x^c = 2\xi_x \sim E_g^{-1}$, while $L_y^c = 2\xi_y$ is significantly smaller than E_g^{-1} for small gaps [Figs. 3(b,c)]. The longitudinal tunneling conductance between leads attached to two d boundaries and through the 1D edge channels conducting along \bar{d} boundaries reads (see ref. [80]) $G_{xx}^{(L_y)}(G_{yy}^{(L_x)}) \rightarrow G_{xx(yy)}^{(\infty)} = Me^2/h$

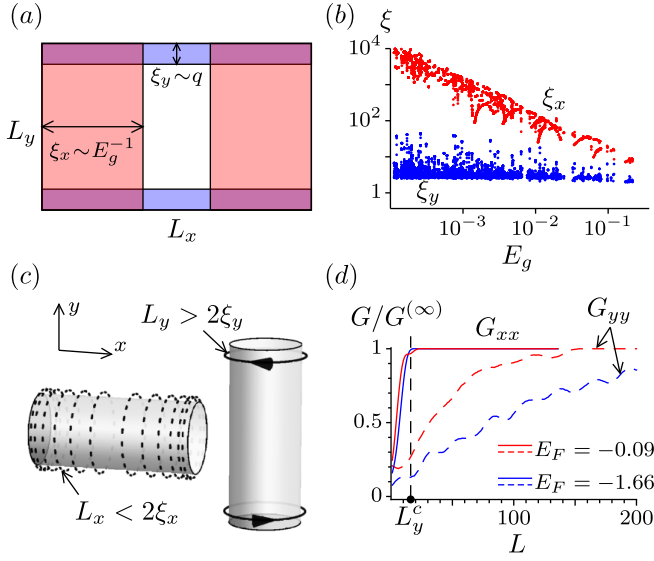


Figure 3. (a) Schematic diagram showing ξ_d of the edge states. (b) $\xi_{x,y}$ vs E_g . Energy of the edge states are set at gap center. Data includes $\phi = p/q$ with coprime p and q , $5 \leq q \leq 149$, and p minimizing $|\phi - (\sqrt{5}-1)/2|$. (c) Schematic diagram shows the effect of anisotropy of the edge states. Edge states in x -periodic system (right cylinder) is localized on the edge, whereas that in y -periodic system (left) are coupled and gapped out when the bulk gap is too small. (d) The ratio $G/G^{(\infty)}$ of the tunneling conductance at finite width to that at infinite width vs the width L when $\phi = 13/21$. $t_x = 1, t_y = 0.7$ for all subgraph.

for sufficiently large $L_{y(x)} > L_y^c$, where M denotes the number of 1D edge channels contributed to the tunneling. Given that $L_x^c \gg L_y^c$ for the small gaps, when the system size $L_x = L_y = L$ with $L_x^c > L > L_y^c$, the edge states localized in the x -boundary (y -boundary) are coupled (decoupled), resulting in $G_{xx}^{(L)}$ (contributed by y -boundary edge states) being significantly larger than $G_{yy}^{(L)}$ [80]. In summary, $G_{yy}^{(L)} < G_{yy}^{(\infty)}$ for the typical small gaps, but $G_{xx}^{(L)} = G_{xx}^{(\infty)}$ is independent of the gap size [Fig. 3(d)], rendering an exotic enhancement of $G_{xx}^{(L)}$ through edge states by AQP. This sharp contrast deeply reflects the different universal scalings (i.e. the power-law and exponential law) of the 2D bulk in x and y directions.

Finite-temperature anisotropic MITs.—When finite temperature T is considered, the system exhibits various MITs tuned by temperature with different E_F . The finite-temperature MITs are defined through $d\sigma/dT = 0$ and can be interpreted using the Boltzmann equation, where the density of states ρ and the square of the group velocity v_d^2 are key parameters. Transport in the x -direction is entirely determined by whether E_F is located in the bulk band or in the gap, similar to previous results at zero temperature [80]. In the y -direction, the system behaves as an insulator at sufficiently low T for large q , except when E_F is in the immediate vicinity of the band-gap boundary, where the product ρv_y^2 is peaked [Fig. 4(a)] [80]. This feature is due to the near flat band configurations in the AQP regime, similar to the results in Fig. 1(c2).

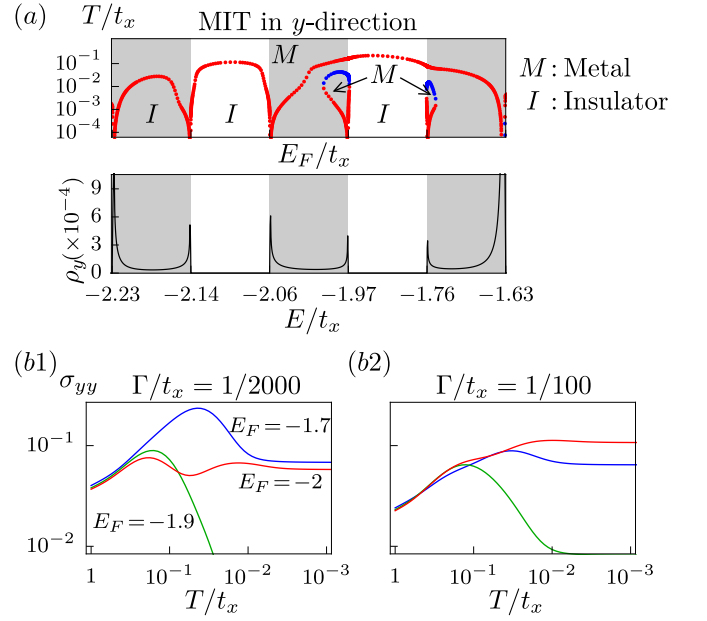


Figure 4. (a) Metal-insulator boundaries (upper panel) for small Γ and the corresponding ρv_y^2 (lower panel). Red (blue) dots denote the MIT temperature T_0 . Gray (white) denotes the region of band (gap). Conductivity vs temperature for (b1) $\Gamma/t_x = 1/2000$ and (b2) $\Gamma/t_x = 1/100$. For all subgraphs, $t_x = 1, t_y = 0.7, \phi = 8/13$.

We numerically find that the MIT in the y -direction approximately occurs at $T \sim \delta$, where δ is the energy difference between E_F and the nearest band-gap boundary [Fig. 4(b1, b2)]. In particular, the loop-like feature in Fig. 4(a) indicates that multiple MITs with T occur at specific Fermi energies, as shown for $E_F = -2$ in Fig. 4(b1), as a consequence of the contribution from peaks of ρv_y^2 at two band-gap boundaries (see Ref. [88] for a detailed explanation). In comparison, for large T the system generally enters metal phase [Fig. 4(a)], similar to the Metal-I phase at large relaxation.

Discussion and conclusion.— We have predicted that the asymptotic quasiperiodicity (AQP) in a 2D anisotropic system host exotic universal wave-packet dynamics, bulk and edge transport phenomena, which have a unified profound mechanism interpreted as the universal scaling laws emerging in the AQP regime. The results unveil new metal-insulator transitions driven by the interplay effect between AQP, relaxation, and finite temperature, which demonstrate nontrivial asymptotic connection to quantum phases in the quasiperiodic limit. The prediction is feasible for experimental study. The lattice with tunable magnetic flux can be experimentally achieved in various systems, such as cold atoms [89–91]. The two main parameters Γ and T can be controlled. For cold atoms, the lowest temperature and relaxation coefficient can be tuned to about 10^{-2} and 10^{-4} of hopping energy, respectively [92]. In solid platforms like quantum dots, these parameters can be as low as 10^{-3} and 10^{-4} , respectively [93–95]. With these parameters our predictions can be well observed by taking $\phi = 8/13$ or $13/21$ [96]. We point out that our predictions can

be studied or directly applied to understand the transport phenomena in the recently highly attractive 2D Moiré materials, in which by adjusting the angle of rotation between the two layers, one can tune moiré materials to be periodic, quasiperiodic, or asymptotically quasiperiodic [54–56, 62–66, 97–99]. Our work opens up an avenue to study the intriguing transport physics with AQP in high dimensions.

Acknowledgement.—We thank Xin-Chi Zhou and Ming Gong for valuable discussions. This work was supported by National Key Research and Development Program of China (No. 2021YFA1400900 and No. 2022YFA1405800), the National Natural Science Foundation of China (Grants No. 12425401, No. 12261160368, No. 12104205, and No. 11921005), and the Innovation Program for Quantum Science and Technology (Grant No. 2021ZD0302000).

Note added.—We recently became aware of a preprint [100] that similarly maps 2D strained Moiré systems with uniform magnetic field to an 1D Aubry-André-Harper model to illustrate the anisotropic transport behavior. Apart from this mapping, our study focuses on the 2D asymptotic quasiperiodic regime, and discovers the novel universal transport phenomena, and the anisotropic MITs. Ref [100] further supports the applicability of our results to the 2D Moiré materials, including various types of lattice configurations such as honeycomb and triangular lattices.

* Corresponding author: wangyc3@sustech.edu.cn

† Corresponding author: xiongjunliu@pku.edu.cn

- [1] M. Y. Azbel, Quantum particle in one-dimensional potentials with incommensurate periods, *Phys. Rev. Lett.* **43**, 1954 (1979).
- [2] S. Aubry and G. André, Analyticity breaking and Anderson localization in incommensurate lattices, *Ann. Israel Phys. Soc.* **3**, 18 (1980).
- [3] G. Roati, C. D’Errico, L. Fallani, M. Fattori, C. Fort, M. Zaccanti, G. Modugno, M. Modugno, and M. Inguscio, Anderson localization of a non-interacting bose-einstein condensate, *Nature* **453**, 7197 (2008).
- [4] S. D. Sarma, S. He, and X. C. Xie, Mobility edge in a model one-dimensional potential, *Phys. Rev. Lett.* **61**, 2144 (1988).
- [5] J. Biddle and S. D. Sarma, Predicted mobility edges in one-dimensional incommensurate optical lattices: an exactly solvable model of Anderson localization, *Phys. Rev. Lett.* **104**, 070601 (2010).
- [6] S. Ganeshan, J. H. Pixley, and S. D. Sarma, Nearest neighbor tight binding models with an exact mobility edge in one-dimensional, *Phys. Rev. Lett.* **114**, 146601 (2015).
- [7] X. Li, X. Li, and S. D. Sarma, Mobility edges in one dimensional bichromatic incommensurate potentials, *Phys. Rev. B* **96**, 085119 (2017).
- [8] F. A. An, E. J. Meier, B. Gadway, Engineering a flux-dependent mobility edge in disordered zigzag chains, *Phys. Rev. X* **8**, 031045 (2018).
- [9] H. P. Lüschen, S. Scherg, T. Kohlert, M. Schreiber, P. Bordia, X. Li, S. D. Sarma, I. Bloch, Single-particle mobility edge in a one-dimensional quasiperiodic optical lattice, *Phys. Rev. Lett.*, **120**, 160404 (2018).
- [10] X. Deng, S. Ray, S. Sinha, G. V. Shlyapnikov, and L. Santos, One-dimensional quasicrystals with power-law hopping, *Phys. Rev. Lett.* **123**, 025301 (2019).
- [11] H. Yao, A. Khoudli, L. Bresque, and L. Sanchez-Palencia, Critical behavior and fractality in shallow one-dimensional quasiperiodic potential, *Phys. Rev. Lett.* **123**, 070405 (2019).
- [12] Y. Wang, X. Xia, L. Zhang, H. Yao, S. Chen, J. You, Q. Zhou, and X.-J. Liu, One dimensional quasiperiodic mosaic lattice with exact mobility edges, *Phys. Rev. Lett.* **125**, 196604 (2020).
- [13] S. Roy, T. Mishra, B. tanatar, and S. Basu, Reentrant localization transition in a quasiperiodic chain, *Phys. Rev. Lett.* **126**, 106803 (2021).
- [14] F. A. An, K. Padavić, E. J. Meier, S. Hegde, S. Ganeshan, J. H. Pixley, S. Vishveshwara, B. Gadway, Interactions and mobility edges: observing the generalized Aubry-André model, *Phys. Rev. Lett.*, **126**, 040603 (2021).
- [15] Y. Wang, J.-H. Zhang, Y. Li, J. Wu, W. Liu, F. Mei, Y. Hu, L. Xiao, J. Ma, C. Chin, S. Jia, Observation of interaction-induced mobility edge in an atomic Aubry-André wire, *Phys. Rev. Lett.* **129**, 103401 (2022).
- [16] A. Padhan, M. K. Giri, S. Mondal, and T. Mishra, Emergence of multiple localization transitions in a one-dimensional quasiperiodic lattice, *Phys. Rev. B* **105**, L220201 (2022).
- [17] Y. Hatsugai and M. Kohmoto, Energy spectrum and the quantum hall effect on the square lattice with next nearest-neighbor hopping, *Phys. Rev. B* **42**, 8282 (1990).
- [18] F. Liu, S. Ghosh, and Y. D. Chong, Localization and adiabatic pumping in a generalized Aubry-André-Harper model, *Phys. Rev. B* **91**, 014108 (2015).
- [19] J. Wang, X.-J. Liu, X. Gao, and H. Hu, Phase diagram of a non-abelian aubry-andré-harper model with p-wave superfluidity, *Phys. Rev. B* **93**, 104504 (2016).
- [20] T. Xiao, D. Xie, Z. Dong, T. Chen, W. Yi, and B. Yan, Observation of topological phase with critical localization in quasiperiodic lattice, *Science Bulletin*, **66**, 2175 (2021).
- [21] Y. Wang, C. Cheng, X.-J. Liu, and D. Yu, Many-body critical phase: extended and nonthermal, *Phys. Rev. Lett.* **126**, 080602 (2021).
- [22] T. Liu, X. Xia, S. Longhi, L. Sanchez-Palencia, Anomalous mobility edges in one-dimensional quasiperiodic models, *SciPost Physics* **12**, 027 (2022).
- [23] Y. Wang, L. Zhang, W. Sun, T.-F. J. Poon, and X.-J. Liu, Quantum phase with coexisting localized, extended, and critical zones, *Phys. Rev. B* **106**, L140203 (2022).
- [24] T. Shimasaki, M. Prichard, H. E. Kondakci, J. E. Pagett, Y. Bai, P. Dotti, A. Cao, T.-C. Lu, T. Grover, D. M. Weld, Anomalous localization and multifractality in a kicked quasicrystal, *arXiv:2203.09442*.
- [25] H. Li, Y.-Y. Wang, Y.-H. Shi, K. Huang, X. Song, G.-H. Liang, Z. Y. Mei, B. Zhou, H. Zhang, J.-C. Zhang, S. Chen, S. Zhao, Y. Tian, Z.-Y. Yang, Z. Xiang, K. Xu, D. Zheng, H. Fan, Observation of critical phase transition in a generalized Aubry-André-Harper model with superconducting circuits, *npj Quantum Information*, **9**, 40 (2023).
- [26] X.-C. Zhou, Y. Wang, T.-F. J. Poon, Q. Zhou, and X.-J. Liu, Exact new mobility edges between critical and localized states, *Phys. Rev. Lett.* **131**, 176401 (2023).
- [27] M. Gonçalves, B. Amorim, E. V. Gactro, P. Riberio, Critical phase dualities in 1D exactly solvable quasiperiodic models, *Phys. Rev. Lett.* **131**, 186303 (2023).
- [28] B. Damski, J. Zakrzewski, L. Santos, P. Zoller, and M. Lewenstein, Atomic base and Anderson glasses in optical lattices, *Phys. Rev. Lett.* **91**, 080403 (2003).

- [29] R. Roth and K. Burnett, Phase diagram of bosonic atoms in two-color superlattices, *Phys. Rev. A* **68**, 023604 (2003).
- [30] T. Roscilde, Bosons in one-dimensional incommensurate superlattices, *Phys. Rev. A* **77**, 063605 (2008).
- [31] X. Deng, R. Citro, A. Minguzzi, and E. Orignac, Phase diagram and momentum distribution of an interaction bose gas in a bichromatic lattice, *Phys. Rev. A* **78**, 013625 (2008).
- [32] G. Roux, T. Barthel, I. P. McCulloch, C. Kollath, U. Schollwöck, and T. Giamarchi, Quasiperiodic bose-hubbard model and localization in one-dimensional cold atomic gases, *Phys. Rev. A* **78**, 023628 (2008).
- [33] V. P. Michal, B. L. Altshuler, and G. V. Shlyapnikov, Delocalization of weakly interacting bosons in a 1d quasiperiodic potential, *Phys. Rev. Lett.* **113**, 045304 (2014).
- [34] H. Yao, T. Giamarchi, and L. Sanchez-Palencia, Lieb-liniger bosons in a shallow quasiperiodic potential: Bose glass phase and fractal mott lobes, *Phys. Rev. Lett.* **125**, 060401 (2020).
- [35] R. Gautier, H. Yao, and L. Sanchez-Palencia, Strongly interacting bosons in a two-dimensional quasicrystal lattice, *Phys. Rev. Lett.* **126**, 110401 (2021).
- [36] Z. Shu, H. Yao, and L. Sanchez-Palencia, Thermodynamic phase diagram of two-dimensional bosons in a quasicrystal potential, *Phys. Rev. Lett.* **130**, 220402 (2023).
- [37] S. Iyer, V. Oganessian, G. Refael, and D. A. Huse, Many-body localization in a quasiperiodic system, *Phys. Rev. B* **87**, 134202 (2013).
- [38] X. Li, S. Ganeshan, J. H. Pixley, and S. D. Sarma, Many-body localization and quantum nonergodicity in a model with a single-particle mobility edge, *Phys. Rev. Lett.* **115**, 186601 (2015).
- [39] R. Modak and S. Mukerjee, Many-body localization in the presence of a single-particle mobility edge, *Phys. Rev. Lett.* **115**, 230401 (2015).
- [40] M. Schreiber, S. S. Hodgman, P. Bordia, H. P. Lüschen, M. H. Fischer, R. Vosk, E. Altman, U. Schneider, and I. Bloch, Observation of many-body localization of interacting fermions in a quasirandom optical lattice, *Science* **349**, 6250 (2015).
- [41] P. Bordia, H. Lüschen, S. Scherg, S. Gopalakrishnan, M. Knap, U. Schneider, and I. Bloch, Probing slow relaxation and many-body localization in two-dimensional quasiperiodic systems, *Phys. Rev. X* **7**, 041047 (2017).
- [42] V. Khemani, D. N. Sheng, and D. A. Huse, Two universality classes for the many-body localization transition, *Phys. Rev. Lett.* **119**, 075702 (2017).
- [43] T. Kohlert, S. Scherg, X. Li, H. P. Lüschen, S. D. Sarma, I. Bloch, and M. Aidelsburger, Observation of many-body localization in a one-dimensional system with a single-particle mobility edge, *Phys. Rev. Lett.* **122**, 170403 (2019).
- [44] A. Lukin, M. Rispoli, R. Schittko, M. E. Tai, A. M. Kaufman, S. Choi, V. Khemani, J. Léonard, and M. Greiner, Probing entanglement in many-body-localized system, *Science* **364**, 6437 (2019).
- [45] M. Kohmoto and J. R. Banavar, Quasiperiodic lattice: Electronic properties, phonon properties, and diffusion, *Phys. Rev. B* **34**, 563 (1986).
- [46] F. Piéchon, Anomalous diffusion properties of wave packets on quasiperiodic chains, *Phys. Rev. Lett.* **76**, 4372 (1996).
- [47] P. Ribeiro, P. Milman, and R. Mosseri, Aperiodic quantum random walks, *Phys. Rev. Lett.* **93**, 190503 (2004).
- [48] Y. B. Lev, D. M. Kennes, C. Klöckner, and D. R. Reichman, Transport in quasiperiodic interacting systems: From superdiffusion to subdiffusion, *Europhysics Letters* **119**, 3 (2017).
- [49] N. F. Mott and W. D. Twose, The theory of impurity conduction, *Advances in physics* **10**, 38 (1961).
- [50] D. Vollhardt and P. Wölfle, Diagrammatic, self-consistent treatment of the Anderson localization problem in $d \leq 2$ dimensions, *Phys. Rev. B* **22**, 4666 (1980).
- [51] R. Carmona, A. Klein, and F. Martinelli, Anderson localization for bernoulli and other singular potentials, *Communications in Mathematical Physics* **108**, 1 (1987).
- [52] E. Abrahams, P. W. Anderson, D. C. Licciardello, and T. V. Ramakrishnan, Scaling theory of localization: Absence of quantum diffusion in two dimensions, *Phys. Rev. Lett.* **42**, 673 (1979).
- [53] F. Wegner, Inverse participation ratio in $2+\epsilon$ dimensions, *Physik B Condensed Matter* **36**, 209 (1980).
- [54] C. R. Dean, L. Wang, P. Maher, C. Forsythe, F. Ghahari, Y. Gao, J. Katoch, M. Ishigami, P. Moon, M. Koshino, T. Taniguchi, K. Watanabe, K. L. Shepard, J. Hone, and P. Kim, Hofstadter's butterfly and the fractal quantum hall effect in moiré superlattices, *Nature* **497**, 598 (2013).
- [55] B. Huang and W. V. Liu, Moiré localization in two-dimensional quasiperiodic systems, *Phys. Rev. B* **100**, 144202 (2019).
- [56] D. Mao and T. Senthil, Quasiperiodicity, band topology, and moiré graphene, *Phys. Rev. B* **103**, 115110 (2021).
- [57] A. Girschik, F. Libisch, S. Rotter, Topological insulator in the presence of spatially correlated disorder, *Phys. Rev. B* **88**, 014201 (2013).
- [58] M. Sbroscia, K. Viebahn, E. Carter, J.-C. Yu, A. Gaunt, and U. Schneider, Observing localization in a 2D quasicrystalline optical lattice, *Phys. Rev. Lett.* **125**, 200604 (2020).
- [59] Y. Fu, J. H. Wilson, J. H. Pixley, Flat topological bands and eigenstate criticality in a quasiperiodic insulator, *Phys. Rev. B* **104**, L041106 (2021).
- [60] T. Okugawa, T. Nag, D. M. Kennes, Correlated disorder induced anomalous transport in magnetically doped topological insulators, *Phys. Rev. B* **106**, 045417 (2022).
- [61] M. Cage, K. Klitzing, A. M. Chang, F. Duncan, M. Haldane, R. B. Laughlin, A. M. M. Pruisken, and D. J. Thouless, The quantum hall effect, *Springer Science & Business Media* (2012).
- [62] B. Hunt, J. D. Sanchez-Yamagishi, A. F. Young, M. Yankowitz, B. J. Leroy, K. Watanabe, M. K. P. J.-H. T. Taniguchi, P. Moon, and R. C. Ashoori, Massive Dirac fermions and Hofstadter butterfly in a van der waals heterostructure, *Science* **340**, 1427 (2013).
- [63] K. Kim, A. DaSilva, S. Huang, B. Fallahzad, S. Larentis, T. Taniguchi, K. Watanabe, B. J. LeRoy, A. H. MacDonald, and E. Tutuc, Tunable moiré bands and strong correlations in small-twist-angle bilayer graphene, *Proceedings of the National Academy of Sciences* **114**, 3364 (2017).
- [64] E. M. Spanton, H. Z. A. A. Zibrov, T. Taniguchi, K. Watanabe, M. P. Zaletel, and A. F. Young, Observation of fractional chern insulators in a van der waals heterostructure, *Science* **360**, 62 (2018).
- [65] Y. Xie, A. T. Pierce, J. M. Park, D. E. Parker, E. Khalaf, P. Ledwith, Y. Cao, S. H. Lee, S. Chen, P. R. Forrester, K. Watanabe, T. Taniguchi, A. Vishwanath, P. Jarillo-Herrero, and A. Yacoby, Fractional chern insulators in magic-angle twisted bilayer graphene, *Nature* **600**, 439 (2021).
- [66] D. E. Parker, T. Soejima, J. Hauschild, M. P. Zaletel, and N. Bultinck, Strain-Induced Quantum Phase Transitions in Magic-Angle Graphene, *Phys. Rev. Lett.* **127**, 027601 (2021).
- [67] N. Mott, Metal-insulator transitions, *CRC Press* (2004).
- [68] Z. Yang, C. Ko, and S. Ramanathan, Oxide electronics utilizing ultrafast metal-insulator transitions, *Annual Review of*

- Materials Research* **41**, 337 (2011).
- [69] D. Jérôme, T. M. Rice, W. Kohn, Excitonic insulator, *Phys. Rev.*, **158**, 462 (1967).
- [70] G. Grüner, The dynamics of charge-density waves, *Rev. Mod. Phys.*, **60**, 1129 (1988).
- [71] G. Grüner, The dynamics of spin-density waves, *Rev. Mod. Phys.*, **66**, 1 (1994).
- [72] B. Spivak, S. A. Kivelson, Phases intermediate between a two-dimensional electron liquid and Wigner crystal, *Phys. Rev. B*, **70**, 155114 (2004).
- [73] C. Liu, T. Kondo, R. M. Fernandes, A. D. Palczewski, E. D. Mun, N. Ni, A. N. Thaler, A. Bostwick, E. Rotenberg, J. Schmalian, S. L. Bud'ko, P. C. Canfield, and A. Kaminski, Evidence for a Lifshitz transition in electron-doped iron arsenic superconductors at the onset of superconductivity, *Nature Physics* **6**, 419 (2010).
- [74] D. LeBoeuf, N. Doiron-Leyraud, B. Vignolle, M. Sutherland, B. J. Ramshaw, J. Levallois, R. Daou, F. Laliberté, O. Cyr-Choinière, J. Change, Y. J. Jo, L. Balicas, R. Liang, D. A. Bonn, W. N. Hardy, C. Proust, and L. Taillefer, Lifshitz critical point in the cuprate superconductor $\text{YBa}_2\text{Cu}_3\text{O}_y$ from high-field Hall effect measurements, *Nature Physics* **7**, 12 (2011).
- [75] F. Gebhard, The Mott Metal-Insulator Transition – Models and Methods, *Springer-Verlag Berlin Heidelberg* (1997).
- [76] S. Kirkpatrick, Percolation and conduction, *Rev. Mod. Phys.*, **45**, 574 (1973)
- [77] J. Villain, Insulating spin glasses, *Zeitschrift für Physik B Condensed Matter*, **33**, 31-42 (1979)
- [78] R. A. Dunlap, The golden ratio and fibonacci numbers, *World Scientific* (1997).
- [79] The Aubry-André-Harper (AAH) model can be written as $H = \sum_j 2V_0 \cos(2\pi\phi j + \phi_0) c_j^\dagger c_j + t_0 (c_j^\dagger c_{j+1} + h.c.)$. V_0, t_0, ϕ_0 are respectively the onsite potential, hopping, and initial phase referred in the maintext. ϕ is irrational in the original AAH model and when it is rational, the model is referred as the “periodic version of AAH model” in the main text. When ϕ is irrational, the critical point is at $V_0 = t_0$, so when V_0 is larger (smaller) than the critical value, the system is localized (extended).
- [80] See supplementary material for the (A) details of numerical analysis of the various scaling law; (B) the detailed theoretic analysis of the scaling laws; (C) Phase diagram in the zero-temperature regime; (D) Details in the scaling law related to the longitudinal conductivity; (E) Details in the edge transport with the analytic derivation of the localization length of the edge; (F) Phase diagram in the finite-temperature regime for both directions and details of the MIT in the y -direction; (G) Characterization of the bulk state wavefunctions and (H) The isotropic case with $t_x = t_y$, which includes [101, 102].
- [81] D. J. Thouless, S. Kirkpatrick, Conductivity of the disordered linear chain, *Journal of Physics C: Solid State Physics* **14**, 235 (1981).
- [82] J. Mitscherling, Longitudinal and anomalous hall conductivity of a general two-band model, *Phys. Rev. B* **102**, 165151 (2020).
- [83] N. Okuma, M. Sato, Non-Hermitian skin effects in Hermitian correlated or disordered systems: quantities sensitive or insensitive to boundary effects and pseudo-quantum-number *Phys. Rev. Lett.*, **126**, 176601 (2021).
- [84] C. R. Dean, A. F. Young, I. Meric, C. Lee, L. Wang, S. Sorgenfrei, K. Watanabe, T. Taniguchi, P. Kim, K. L. Shepard, and J. Hone, Boron nitride substrates for high-quality graphene electronics, *Nature Nanotechnology*, **5**, 722 (2010).
- [85] Y. Zhang, Y.-W. Tan, H. L. Stormer, and P. Kim, Experimental Observation of Quantum Hall Effect and Berry’s Phase in Graphene, *Nature* **438**, 201 (2005).
- [86] A. J. Daley, Quantum trajectories and open many-body quantum systems, *Adv. Phys.* **63**, 77 (2014).
- [87] G. Barontini, R. Labouvie, F. Stubenrauch, A. Vogler, V. Guarnera, and H. Ott, Controlling the Dynamics of an Open Many-Body Quantum System with Localized Dissipation, *Phys. Rev. Lett.* **110**, 035302 (2013).
- [88] Consider the Fermi energy $E_F = -2$, close to the peak located at the gap boundary $E = -1.97$ [see Fig. 4(a)]. Initially, as the temperature T increases, the particles are excited to the states at the peak $E = -1.97$, causing σ_{yy} to increase and thus $d\sigma_{yy}/dT > 0$, manifesting an insulator. After the states at the peak $E = -1.97$ are nearly fully occupied, σ_{yy} will decrease with increasing T , turning the system into a metal with $d\sigma_{yy}/dT < 0$. Further increasing T leads to unoccupation of the states at the lower peak $E = -2.06$, which accordingly increases the hole contribution in this peak and enhance σ_{yy} again, rendering an insulator with $d\sigma_{yy}/dT > 0$. Finally, the system will reenter metal phase when T increases to high enough, similar to the regime with large Γ at zero temperature. The underlying mechanism of the multiple metal-insulator transitions around $E_F = -1.76$ can be similarly analyzed with the hole charge carrier picture. The absence of loop-like feature around $E = -2.06, -2.14$ is because the peaks of ρv_y^2 at the two gap boundaries are large such that the metal phase at high T extends to the very low T regime.
- [89] M. Aidelsburger, M. Atala, M. Lohse, J. T. Barreiro, B. Paredes, and I. Bloch, Realization of the Hofstadter Hamiltonian with ultracold atoms in optical lattices, *Phys. Rev. Lett.* **111**, 185301 (2013).
- [90] H. Miyake, G. A. Siviloglou, C. J. Kennedy, W. C. Burton, and W. Ketterle, Realizing the Harper Hamiltonian with laser-assisted tunneling in optical lattices, *Phys. Rev. Lett.* **111**, 185302 (2013).
- [91] Y. Bai and D. M. Weld, Tessellated phase diagram and extended criticality in driven quasicrystals and quantum Hall matter, [arXiv:2406.01445](https://arxiv.org/abs/2406.01445).
- [92] S. Krinner, D. Staler, D. Hushman, J.-P. Brantut, T. Esslinger, Observation of quantized conductance in neutral matter, *Nature* **517**, 64-67 (2015).
- [93] C. Volk, C. Neumann, S. Kazarski, S. Fringes, S. Engels, F. Haupt, A. Müller, and C. Stampfer, Probing relaxation times in graphene quantum dots, *Nature Communication* **4**, 1 (2013).
- [94] P. Barthelemy, L. M. K. Vandersypen, Quantum Dot Systems: a versatile platform for quantum simulation, *Annalen der Physik* **525**, 10-11 (2013).
- [95] D. Wei, H.-O. Li, G. Cao, G. Luo, Z.-X. Zheng, T. Tu, M. Xiao, G.-C. Guo, H.-W. Jiang, G.-P. Guo, Tuning inter-dot tunnel coupling of an etched graphene double quantum dot by adjacent metal gates, *Scientific reports* **3**, 3175 (2013).
- [96] We note that although we use the Fibonacci ratio p_n/q_n , our results are flexible. Indeed, our results are primarily determined by q_n , as long as the ratio is finite and the limit is irrational. Then, for finite n the value p_n can vary within a certain range, such as $8/13$ being written as $7/13$ or $9/13$, without affecting our conclusions. This makes our predictions be of high feasibility for experimental realization.
- [97] A. Weston, *Introduction to 2-Dimensional Materials and Moiré Superlattices*, Springer Theses. Springer, Cham. (2022).
- [98] G. Trambly de Laissardiére, D. Mayou, and L. Magaud, Numerical studies of confined states in rotated bilayers of graphene, *Phys. Rev. B* **86**, 125413 (2012).

- [99] S. J. Ahn, P. Moon, T.-H. Kim, H.-W. Kim, H.-C. Shin, E. H. Kim, H. W. Cha, S.-J. Kahng, P. Kim, M. Koshino, Y.-W. Son, C.-W. Yang, and J. R. Ahn, Dirac electrons in a dodecagonal graphene quasicrystal, *Science* **361**, 782 (2018).
- [100] N. Paul, P. J. D. Crowley, and Liang Fu, Directional Localization from a Magnetic Field in Moiré systems, *Phys. Rev. Lett.* **132**, 246402 (2024).
- [101] J. Sokoloff, Unusual band structure, wave functions and electrical conductance in crystals with incommensurate periodic potentials, *Physics Reports* **126**, 189 (1985).
- [102] R. Resta and S. Sorella, Electron localization in the insulating state, *Phys. Rev. Lett.* **82**, 370 (1999).

Supplementary Material: Anomalous universal quantum transport in 2D asymptotic quasiperiodic system

In this supplementary material, we present (A) the numerical analysis of the bulk properties over q , and (B) their theoretical basis. (C) The zero-temperature phase diagram is shown for different values of q . We also include (D) the details of the longitudinal conductivity, with a consistency check of the related scaling laws, and (E) the transverse conductivity along with the related edge transport, including the Chern number of the gaps and an analytic proof of the localization length ξ_y . Then, we demonstrate that (F) in the x -direction, our system indeed behaves conventionally in the finite temperature regime, and we provide some details of the metal-insulator transition (MIT) in the y -direction. Finally, we discuss (G) the use of other quantities to characterize the localization and extension behavior of the wave function, and (H) the interesting physical phenomena at the isotropic point $t_x = t_y$.

A. Numerical analysis of the scaling laws of bulk properties

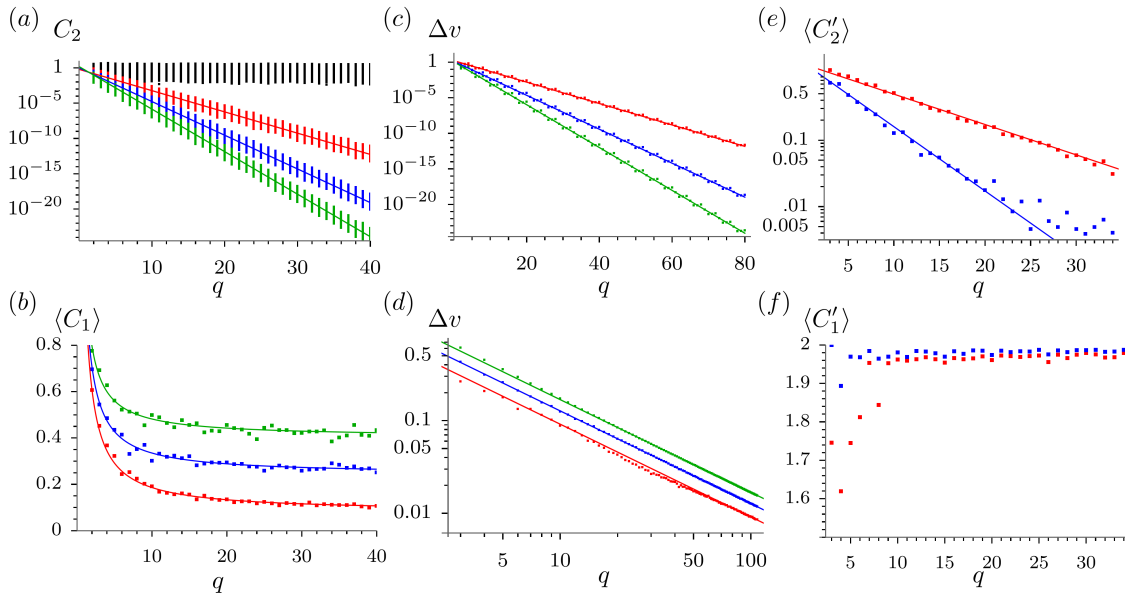


Figure S1. (a) C_2 vs q . The points denote data with varying p and initial wavefunction $\psi(0)$. Solid lines represent the fitting of the mean $\langle C_2 \rangle \propto (t_y/t_x)^q$. Red, blue and green represent the data with $t_y/t_x = 1/2, 1/3$ and $1/4$ respectively. Black dots represent C_1 , showing that C_1 only depends weakly on q . (b) $\langle C_1 \rangle$ vs q . Points and solid line represent the data and their fitted line respectively. Red, blue and green represent the data with $t_y/t_x = 0.9, 0.7$ and 0.5 , respectively. The general formula of the fitted lines is $0.807(t_x - t_y) + 1.11\sqrt{t_y t_x}/q$ (c) Δv vs q for $t_y < t_x$. Red, blue and green datas are calculated with $t_y/t_x = 1/2, 1/3$ and $1/4$ respectively, showing $\Delta v \propto (t_y/t_x)^{q/2}$. (d) Δv vs q for $t_y > t_x$. Red, blue and green dots and fitted lines represent $t_y/t_x = 5, 2$ and $10/7$ respectively, showing $\Delta v \propto q^{-1}\sqrt{t_x t_y}$. (e) $\langle C'_2 \rangle$ vs q for $t_y < t_x$. Red and blue dots and fitted lines represent $t_y/t_x = 0.9$ and 0.8 respectively, showing $\langle C'_2 \rangle \propto (t_x/t_y)^q$ (f) $\langle C'_1 \rangle$ vs q for $t_y > t_x$. Red and blue dots and fitted lines represent $t_y/t_x = 0.9^{-1}$ and 0.8^{-1} respectively, showing $\langle C'_1 \rangle$ does not depend on q for sufficiently large q .

In this section, we present data concerning the numerical analysis of the scaling laws of different parameters of bulk transport with respect to the quantifier of asymptotic quasiperiodicity, q . As described in the main text, C_2 depends on p and the initial wavefunction $\psi(0)$. For each q , we generate random values of p , which is coprime with q , and $\psi(0)$ to form the data points in Fig. S1(a). We note that the most significant correlation with C_2 is q , while p and $\psi(0)$ have minimal effect, so it is natural to consider the average of C_2 , $\langle C_2 \rangle$, over p and $\psi(0)$. From the fitted lines, we establish that $\langle C_2 \rangle \sim t_x(t_y/t_x)^q$. Similarly, we also establish the power-law dependence on q , with $\langle C_1 \rangle \sim 0.807(t_x - t_y) + 1.11q^{-1}\sqrt{t_y t_x}$ [Fig. S1(b)].

The average group velocity, whose exact formula is not shown in the main text, is defined as $\tilde{v}_d(q) = g(q)^{-1} \sum_{m,p} |v_{k_{xM}, k_{yM}}^{(m,p/q,d)}|$, where $v_{k_{xM}, k_{yM}}^{(m,p/q,d)}$ is the group velocity of the m th band in the d -direction of the system at $\phi = p/q$, with $k_x = k_{xM}, k_y = k_{yM}$. Here, k_{xM} and k_{yM} denote the quasi-momentum that corresponds to the maximum group velocity. The normalization constant is given by $g(q) = q\phi(q)$, where $\phi(q)$ is the number of integers less than q that are coprime with q . According to [S1], the total bandwidth of the system is $4(t_y - t_x)$ for infinite q and $t_y > t_x$. Therefore, the mean group

velocity is $4(t_y - t_x)/q \times (\pi/q)^{-1} = 4/\pi \times (t_y - t_x)$, since the system is periodic when $k \rightarrow 2\pi/q + k$. Similar to the above numerical analysis, we averaged the velocities over p and bands, and recovered the numerical relation between $\Delta v = \tilde{v}_y - \tilde{v}_y^{(\infty)}$ and q [Fig. S1(c,d)].

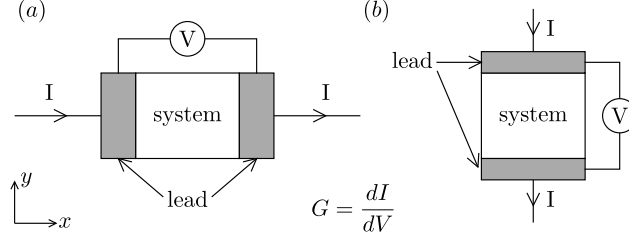


Figure S2. (a,b) Schematic diagrams showing how the tunneling conductance $G_{xx(yy)}$ is obtained from the current I and the voltage V .

Lastly, we propose employing the real-space longitudinal tunneling conductance $G_{xx(yy)}$ in the $x(y)$ direction to detect bulk transport. This conductance is calculated numerically using non-equilibrium Green's function in a real-space system of size $L_y(L_x)$ with two leads at the ends [Fig. S2]. We find that the conductance $G_{xx(yy)}$ in the $x(y)$ direction satisfies

$$G_{xx} = C'_1 L_y; G_{yy} = \begin{cases} C'_2 L_x & \text{for rational } \phi \\ C'_3 & \text{for irrational } \phi \end{cases}, \quad (\text{S1})$$

where numerical analysis shows that $\langle C'_1 \rangle$ is of order 1 and that $\langle C'_2 \rangle \sim \tilde{C}'_2 (t_y/t_x)^q$ [Fig. S1(e,f)]. Here $C'_{1(2)}$ depends on p and Fermi energy E_F . For each q , we compute the average of G_{xx}/L_y or G_{yy}/L_x over p and over random E_F that cuts through the bulk. Notably, for G_{xx} and G_{yy} in the case of rational ϕ , the proportionality of the system size indicates the presence of bulk transport in the system. The similar exponential dependence on q suggests a comparable role of q in the calculation of real-space conductance.

B. Theoretic basis of the scaling law of $\langle C_2 \rangle$ and Δv

In this section, we discuss the theoretical basis for the exponential decay of $\langle C_2 \rangle$ and Δv with respect to q , as well as the additional $1/2$ factor in the exponent of the scaling of Δv . We begin by showing the similarity between Hamiltonians when Fourier-transformed in a single direction versus when Fourier-transformed in two directions. When we choose the A_d gauge, the Hamiltonian can be Fourier transformed in the d -direction, i.e.,

$$\begin{aligned} H &= \sum_{k_x} H_{1D}(k_x) = \sum_{k_x, j_y} 2t_x \cos(k_x - 2\pi\phi j_y) c_{k_x j_y}^\dagger c_{k_x j_y} + (t_y c_{k_x, j_y+1}^\dagger c_{k_x j_y} + h.c.) \quad \text{for } A_x \text{ gauge,} \\ H &= \sum_{k_y} H_{1D}(k_y) = \sum_{k_y, j_x} 2t_y \cos(k_y + 2\pi\phi j_x) c_{j_x k_y}^\dagger c_{j_x k_y} + (t_x c_{j_x+1, k_y}^\dagger c_{j_x k_y} + h.c.) \quad \text{for } A_y \text{ gauge.} \end{aligned} \quad (\text{S2})$$

For rational ϕ , the Hamiltonian can be further Fourier transformed in the \bar{d} -direction, i.e.,

$$\begin{aligned} H &= \sum_{k_x, k_y} \mathcal{H}_{A_x}(k_x, k_y) = \sum_{k_x, k_y} 2t_y \cos(k_y) c_{k_x k_y}^\dagger c_{k_x k_y} + (t_x e^{ik_x} c_{k_x k_y}^\dagger c_{k_x, k_y-2\pi\phi} + h.c.) \quad \text{for } A_x \text{ gauge,} \\ H &= \sum_{k_x, k_y} \mathcal{H}_{A_y}(k_x, k_y) = \sum_{k_x, k_y} 2t_x \cos(k_x) c_{k_x k_y}^\dagger c_{k_x k_y} + (t_y e^{ik_y} c_{k_x k_y}^\dagger c_{k_x+2\pi\phi, k_y} + h.c.) \quad \text{for } A_y \text{ gauge,} \end{aligned} \quad (\text{S3})$$

which can be rewritten into a form resembling the periodic AAH model as mentioned in the main text:

$$\begin{aligned} \mathcal{H}_{A_x} &= \Psi_{k_x, \phi}^\dagger [2t_y D_\phi(k_y) + (t_x e^{-ik_x} M_1 + h.c.)] \Psi_{k_x, \phi}, \\ \mathcal{H}_{A_y} &= \Psi_{-\phi, k_y}^\dagger [2t_x D_{-\phi}(k_x) + (t_y e^{-ik_y} M_1 + h.c.)] \Psi_{-\phi, k_y}, \end{aligned} \quad (\text{S4})$$

where $\phi = p/q$, $2\pi\phi$ is the momentum spacing, $\Psi_{k_x, \phi} = (c_{k_x k_y}, c_{k_x, k_y-2\pi\phi}, \dots, c_{k_x, k_y-2\pi(q-1)\phi})^T$, $\Psi_{-\phi, k_y} = (c_{k_x k_y}, c_{k_x+2\pi\phi, k_y}, \dots, c_{k_x+2\pi(q-1)\phi, k_y})^T$, $D_\phi(k) = \text{diag}(\cos k, \cos(k - 2\pi\phi), \dots, \cos[k - 2\pi(q-1)\phi])$ and M_1 is a circulant matrix with $c_1 = 1$, meaning all elements on the lower diagonal and at the top-right corner are 1, with all others being

0. We note that the Hamiltonians \mathcal{H}_{A_x} and \mathcal{H}_{A_y} are explicitly related by a gauge transformation $\mathcal{H}_{A_x} = U^\dagger \mathcal{H}_{A_y} U$, where $U = (v_0, v_1, \dots, v_{q-1})$ and $v_n = (1, e^{i2\pi n\phi}, e^{i4\pi n\phi}, \dots, e^{i2(q-1)\pi n\phi})^T$. Therefore, in the main text, we simplify the notation by omitting the subscript in \mathcal{H} in the corresponding expression. The \cos function in H_{1D} with the A_x gauge indicates that the eigenfunction decays exponentially in the y -direction for $t_y < t_x$, as the geometric mean of its diagonal terms satisfies

$$\mathbf{G} \stackrel{\text{def}}{=} \prod_{k=0}^{2\pi} |2t_x(\cos k - r)|^{1/(2\pi)} \stackrel{\text{def}}{=} \exp \left[\frac{1}{2\pi} \int_0^{2\pi} dk \log |2t_x(\cos k - r)| \right] = t_x \quad (\text{S5})$$

for $1 > r > -1$. Therefore, when $t_y < t_x$ the off-diagonal terms can be treated as perturbation for sufficiently large q , where the continuous integral accurately represents the discrete geometric mean. Thus, the effective hopping of a charge carrier across a full unit cell is proportional to $t_{\text{eff}} = t_x (t_y/t_x)^q$, which matches the scaling of $\langle C_2 \rangle$.

Secondly, the maximum velocity in the y -direction, v_y , of each band actually corresponds to the maximum velocity of \mathcal{H}_{A_y} over k_x and k_y . This is proportional to the maximum bandwidth of the \mathcal{H}_{A_y} gauge when treating k_x as a parameter and k_y as quasi-momentum. To achieve maximal bandwidth, k_x should be tuned so that some diagonal terms of \mathcal{H}_{A_y} are equal, thereby minimizing the perturbation effect of the off-diagonal terms and maximizing the bandwidth in the y -direction. For example, if $\phi = 5/8$ and $k_x = 0$, then the second and sixth diagonal terms of \mathcal{H}_{A_y} are the same, i.e., $2t_x \cos(2 \times 5\pi/4) = 2t_x \cos(6 \times 5\pi/4) = 0$. Thus, the charge carrier with maximum transport power hops from the second to the sixth site, and then to the second site in the next unit cell, completing a period. This motion results in the bandwidth and the maximum velocities being of the order of $(t_y/t_x)^4 = (t_y/t_x)^{q/2}$. To generalize this result, we assume the diagonal terms to be $V_i(k_x)$, where i indicates the i th diagonal term, and the geometric mean of V is 1 (which can be adjusted by absorbing extra factors into t_x). There are a total of q diagonal terms, with the index i having a period of q . If for some k_x , $V_{i_1}(k_x) = V_{i_2}(k_x) = \dots = V_{i_n}(k_x) = V_{i_1+q}(k_x) = V_0$ with $i_1 + q \geq i_n \geq \dots \geq i_1$, then the bandwidth $E_{b,y}$ in the y -direction of the bands with $E \approx V_0$ satisfies

$$E_{b,y} = \gamma \times \begin{cases} t_x (t_y/t_x)^{M_{n/2} - m_{n/2} - 1} & \text{for } n \text{ is even} \\ t_x (t_y/t_x)^{q - 2m_{(n-1)/2}} & \text{for } n \text{ is odd,} \end{cases} \quad (\text{S6})$$

where γ is some parameter of order 1. M_j (m_j) represents the maximum (minimum) of the sums of j items chosen from the set $\{z_1 = i_2 - i_1, z_2 = i_3 - i_2, \dots, z_n = i_1 + q - i_n\}$. The chosen items $z_{l_1}, z_{l_2}, \dots, z_{l_j}$ must satisfy the following conditions: (i) $|l_\alpha - l_\beta| > 1$ for all $1 \leq \alpha, \beta \leq j$, (ii) if $l_\alpha = 1$, then $l_\beta \neq n$ for all β , and (iii) if $l_\alpha = n$, then $l_\beta \neq 1$ for all β . For example, when $n = 7$, $M_3 = \max\{z_1 + z_3 + z_5, z_1 + z_3 + z_6, z_1 + z_4 + z_6, z_2 + z_4 + z_6, z_2 + z_4 + z_7, z_2 + z_5 + z_7, z_3 + z_5 + z_7\}$, and $m_2 = \min\{z_1 + z_3, z_1 + z_4, z_1 + z_5, z_1 + z_6, z_2 + z_4, z_2 + z_5, z_2 + z_6, z_2 + z_7, z_3 + z_5, z_3 + z_6, z_3 + z_7, z_4 + z_6, z_4 + z_7, z_5 + z_7\}$. Thus, the average of the maximal bandwidth is primarily determined by the case where $z_1 = z_2 = \dots = z_n = q/n$, and then

$$\tilde{v}_y \sim t_x (t_y/t_x)^{q/n}, \quad (\text{S7})$$

where $n = 2$ for the \cos potential considered in our work.

C. Zero temperature phase diagram for different q

In this section, we present the generic phase diagrams at zero temperature for $\phi = 8/13$ and $\phi = 13/21$ [Fig. S3(a,b)]. We note that for $\phi = 13/21$, the region M_2 is reduced, consistent with the discussion in the main text. It is also noteworthy that Γ_{c1} is essentially independent of ϕ , whereas Γ_{c2} is reduced by a factor of 10 to 30 when q changes from 13 to 21, consistent with the scaling law $\Gamma_{c2}/t_x \sim (t_y/t_x)^q$.

D. Details in longitudinal conductivity

In this section, we discuss the details of the calculation of the Kubo formula when applied to the longitudinal conductivity. We first introduce the general Kubo formula at zero temperature:

$$\sigma_{dd'} = \lim_{\omega \rightarrow 0} \frac{ie^2}{\omega \hbar} \int \frac{dk_0}{2\pi} \frac{d^d k}{(2\pi)^d} \text{tr} \left[\left(G_{ik_0+iq_0} |_{i q_0 \rightarrow \omega+i0^+} - G_{ik_0} \right) \frac{d\mathcal{H}}{dk_{d'}} G_{ik_0} \frac{d\mathcal{H}}{dk_d} \right] \quad (\text{S8})$$

$$= \frac{e^2}{\hbar} \int \frac{d^d k}{(2\pi)^d} \text{tr} \left[(G_0^+ - G_0^-) \frac{d\mathcal{H}}{dk_{d'}} G_0^- \frac{d\mathcal{H}}{dk_d} - i \int dk_0 \left(G_{ik_0}^{\text{sgn}(k_0)} \right)^2 \frac{d\mathcal{H}}{dk_{d'}} G_{ik_0}^{\text{sgn}(k_0)} \frac{d\mathcal{H}}{dk_d} \right], \quad (\text{S9})$$

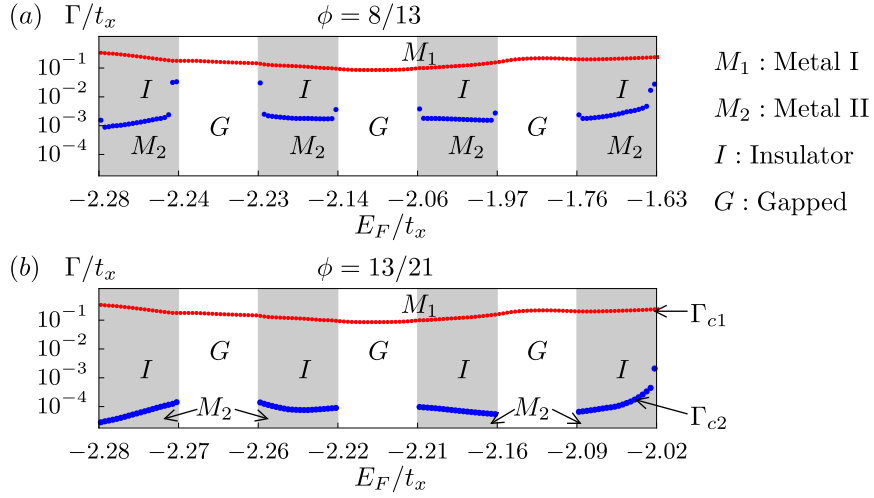


Figure S3. Phase diagrams. The parameters chosen are $t_y = 0.7$ and $t_x = 1$ for the cases (a) $\phi = 8/13$ and (b) $\phi = 13/21$. (b) clearly shows a smaller M_2 region and a larger I region compared to (a).

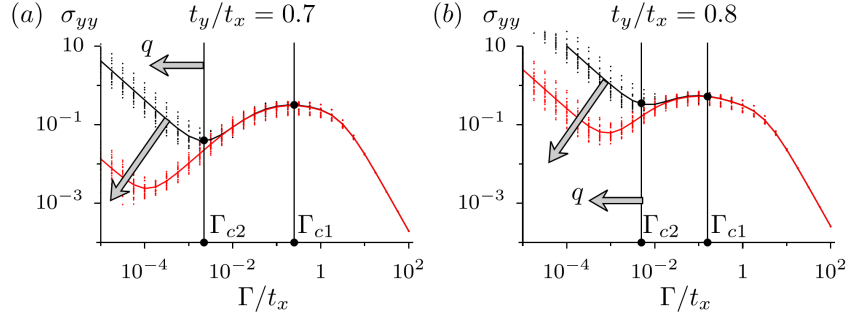


Figure S4. Generic behavior of the longitudinal conductivity σ_{yy} at different Fermi energies located in the bulk vs Γ . The dots represent Fermi energies chosen at the centers, as well as the upper and lower quartiles of all bands, showing similar scaling properties. The lines represent the mean of the calculated σ_{yy} . Black (red) represents the data for $\phi = 8/13$ ($13/21$).

where $G_{ik_0} = (ik_0 + \mu + i\Gamma \text{sgn } k_0 - \mathcal{H})^{-1}$, $G_{ik_0}^{\pm} = (ik_0 + \mu \pm i\Gamma - \mathcal{H})^{-1}$ and Γ is the finite relaxation rate, assumed to be independent of momentum and band. When $d = d'$, the above expression simplifies to

$$\sigma_{dd} = \frac{e^2}{h} \times \Re \left\{ \int \frac{d^2k}{(2\pi)^2} \text{tr} \left[(G_0^+ - G_0^-) \frac{d\mathcal{H}}{dk_d} G_0^- \frac{d\mathcal{H}}{dk_d} \right] \right\}, \quad (\text{S10})$$

where \Re represents the real part of the given expression. The scaling of the conductivity σ_{yy} in the three universal regions, metal I, metal II and insulator, follows $\sigma_{yy} \sim \Gamma^{-1,1,-2}$, respectively. We provide a more detailed numerical analysis below. As shown in Fig. S4, we calculate σ_{yy} using multiple Fermi energies to support our claim about the scaling in the insulating region and the transition points. We further verify this claim by calculating the asymptotic behaviors for both $\Gamma \rightarrow 0$ and $\Gamma \rightarrow \infty$. Specifically, for $\Gamma \rightarrow \infty$,

$$\sigma_{yy}(\Gamma \rightarrow \infty) = \frac{2e^2}{h\Gamma^2} \int \frac{dk_x}{2\pi} \frac{dk_y}{2\pi} \text{tr} \left(\frac{d\mathcal{H}}{dk_y} \frac{d\mathcal{H}}{dk_y} \right) = 4t_y^2 \Gamma^{-2}. \quad (\text{S11})$$

For $\Gamma \rightarrow 0$,

$$\begin{aligned}
\sigma_{yy}(\Gamma \rightarrow 0) &= \frac{e^2}{h\Gamma} \int \frac{dk_x}{2\pi} \frac{dk_y}{2\pi} \sum_b \delta(\epsilon_b(k_x, k_y) - \mu) \left(\frac{\partial \epsilon_b}{\partial k_x} \right)^2 \\
&= \frac{e^2}{h\Gamma} \frac{q}{\pi} \times \left| \Im \left\{ \left(\frac{df}{d\mu} \right)^{-1} \sqrt{\frac{1}{4t_x^{2q} - 8t_x^q t_y^q + 4t_y^{2q} - f^2}} \left[(4t_x^{2q} - 8t_x^q t_y^q + 4t_y^{2q} - f^2) E(\mathfrak{F}_{f,t_x,t_y,q}) \right. \right. \right. \\
&\quad \left. \left. \left. - 2(2t_y^q - f)(2t_y^q - 2t_x^q + f) K(\mathfrak{F}_{f,t_x,t_y,q}) + 8t_y^q f \Pi \left(\frac{2t_x^q + 2t_y^q + f}{2t_y^q - 2t_x^q + f}, \mathfrak{F}_{f,t_x,t_y,q} \right) \right] \right\} \right| \\
&= \frac{e^2 t_x}{h\Gamma} \frac{q}{\pi} \times \left| \Im \left\{ \left(\frac{df'}{d\mu'} \right)^{-1} \sqrt{\frac{1}{(1-r)^2 - f'^2}} \left[((1-r)^2 - f'^2) E(\mathfrak{F}_{f,t_x,t_y,q}) \right. \right. \right. \\
&\quad \left. \left. \left. - 2(r-f')(r-1+f') K(\mathfrak{F}_{f,t_x,t_y,q}) + f' \Pi \left(1 + \frac{2r}{r-1+f'}, \mathfrak{F}_{f,t_x,t_y,q} \right) \right] \right\} \right| \\
&= \frac{e^2 t_x}{h\Gamma} \frac{qr^2}{2\sqrt{1-f'^2}} \left(\frac{df'}{d\mu'} \right)^{-1} + O(r^3), \tag{S12}
\end{aligned}$$

where ϵ_b is the energy of the b th band, $\mathfrak{F}_{f,t_x,t_y,q} = (f^2 - 4t_x^{2q} - 8t_x^q t_y^q - 4t_y^{2q}) / (f^2 - 4t_x^{2q} + 8t_x^q t_y^q - 4t_y^{2q})$, $f = \det(\mathcal{H}(\pi/2q, \pi/2q) - \mu I)$, $f' = f/t_x^q$, $\mu' = \mu/t_x$ and $r = t_y^q/t_x^q$, which is small when $t_y < t_x$ and $q \gg 1$. E, K and Π are the elliptic functions of the first, second and third kinds, respectively. The quantity $df'/d\mu'$ is of the order of q , so in this limit, $\sigma \sim (t_y/t_x)^{2q} t_x \Gamma^{-1}$. A consistency check can be performed by comparing the five scalings behaviors: three from the regions of σ and two from the critical relaxation rates $\Gamma_{c1,c2}$,

$$\sigma_{yy,M_1} \sim 4t_y^2 \Gamma^{-2}, \sigma_{yy,M_2} \sim t_x (t_x/t_y)^{2q} \Gamma^{-1}, \sigma_{yy,I} \sim \Gamma, \Gamma_{c1} \sim t_y, \Gamma_{c2} \sim t_x (t_x/t_y)^q. \tag{S13}$$

Specifically, the consistency can be observed by noting that both Γ_{c1} and σ_{yy,M_1} are independent of q , therefore $\sigma_{yy,I}$ is also independent of q . Then, by comparing the scaling of σ_{yy,M_2} and $\sigma_{yy,I}$, one can independently approximate Γ_{c2} , which is consistent with the result of the numerical analysis, further verifying the numerically derived scalings.

E. Details in transverse conductivity and edge transport

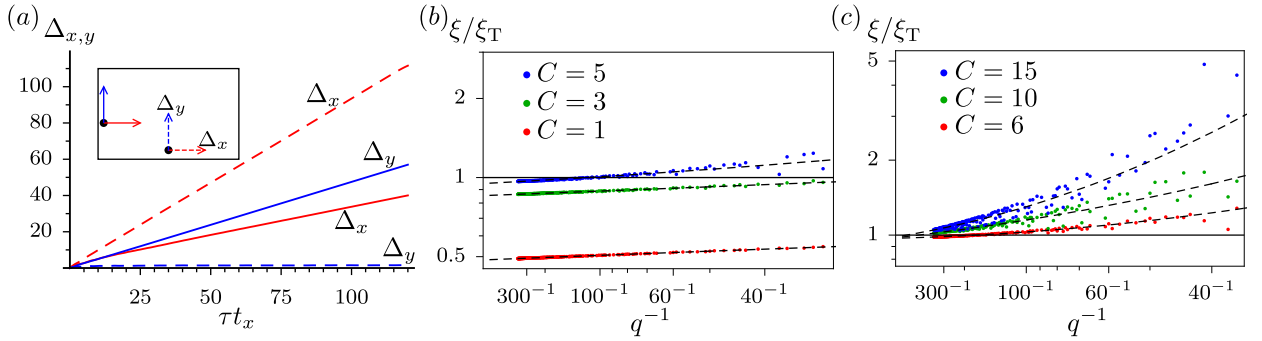


Figure S5. (a) DMSDs vs time. Solid (dashed) lines represent DMSDs when the initial position is at the x -boundary (or y -boundary). Red (blue) lines represent DMSDs in the x -direction (or y -direction). $\phi = (\sqrt{5} - 1)/2$. (b,c) The ratio of the numerically obtained w to the theoretically obtained w_T . The energies across q are chosen at the centers of gaps where the Chern number remains the same. p is chosen such that p/q is closest to $(\sqrt{5} - 1)/2$.

In this section, we discuss the wavepacket dynamics at the edge, the transverse conductivity, and the analytic derivation of the localization length of edge states. For the wavepacket dynamics, we consider DMSDs with the initial position r_0 at the edge. The transport behavior when r_0 is located at the x -boundary is qualitatively different from that at the y -boundary: Both f_x and f_y is diffusive when r_0 is at the x -boundary, while f_x is diffusive and f_y is localized when r_0 is located at the y -boundary, as shown in Fig. S5(a). The implication is that the topological edge states are unaffected by the incommensurate flux ϕ , even when the bulk is localized in one direction. Thus, DMSDs along the edge indicate that the edge is always diffusive, while the DMSDs perpendicular to the edge are still influenced by the bulk displacement function.

Regarding the transverse conductivity σ_{xy} , according to the Kubo's formula given in the main text, it simplifies in the limit as $\Gamma \rightarrow 0$:

$$\sigma_{xy} = \frac{e^2}{h} \int \frac{dk_x dk_y}{(2\pi)^2} \Im \left[\sum_{nm} \frac{\left(\psi_n^* \frac{d\mathcal{H}}{dk_x} \psi_m \psi_m^* \frac{d\mathcal{H}}{dk_y} \psi_n \right)}{(E_n - E_m)^2} \right], \quad (\text{S14})$$

where $\psi_{n(m)}$ denotes the wavefunction of the filled (unfilled) bands. When the Fermi level is located at the gap, the result is proportional to the Chern number of the bands involved. For an arbitrary rational ϕ , the Chern number of the n th band, $C_{p/q}^{(n)}$, is

$$C_{p/q}^{(n)} = \left(p_{\text{mod } q}^{-1} n (1 - \delta_{n,q/2}) + \left\lfloor \frac{q}{2} \right\rfloor \right)_{\text{mod } q} - \left(p_{\text{mod } q}^{-1} (n-1) (1 - \delta_{n-1,q/2}) + \left\lfloor \frac{q}{2} \right\rfloor \right)_{\text{mod } q}, \quad (\text{S15})$$

where the subscript $\text{mod } q$ indicates that the number is calculated in the field of $\mathbb{Z}/q\mathbb{Z}$ (for example, $3_{\text{mod } 13}^{-1} = 9$). Therefore, for all rational ϕ , the edge states continue to exist.

However, even when the edge states exist, their wavefunctions show qualitative differences. For the edge along y , the edge state penetrates into the bulk with a localization length proportional to the gap width E_g , whereas for the edge along x , the localization length of the edge state does not depend on the gap width. We can see this analytically through the following calculation. To begin, we note that the system can be viewed as having a unit cell with q sites, so we can calculate the edge wavefunction using the ansatz $c_{i\alpha} = \lambda^i c_{0\alpha}$, where $\alpha = 0, 1, \dots, q-1$. Then the parameter λ satisfies $\det(-B(k) + \lambda(E - H(k) - \lambda B^\dagger(k))) = 0$, where $B(k)$ is a $q \times q$ matrix describing the hopping from i to $i+1$, and $H(k)$ is a matrix describing the onsite potential. Now, for the x -boundary

$$\lambda_{\pm} = \frac{t_x^{-q}}{2} \left((-1)^q f_{p,q} - 2t_y^q \cos(k_y q) \pm \sqrt{f_{p,q}^2 - 4t_x^{2q} + 4t_y^q \cos(k_y q) (t_y^q \cos(k_y q) - (-1)^q f_{p,q})} \right) \quad (\text{S16})$$

$$= \tilde{f} \pm \sqrt{\tilde{f}^2 - 1}, \quad (\text{S17})$$

where $f_{p,q} = f_{p,q}(e, t_x, t_y)$ is the part of $\det(\mathcal{H} - eI)$ that is independent of k_x and k_y , and $\tilde{f} = t_x^{-q}/2 \times ((-1)^q f_{p,q} - 2t_y^q \cos(k_y q))$. Since f is a continuous function of e , for a sufficiently small gap, the value of f can be approximated by $f_{t/b}$, the value at the top or bottom of the band. Since the top or bottom of the band occurs only at $(k_x, k_y) = (n\pi/q, m\pi/q)$ (where n and m are integers), and $\det(\mathcal{H} - eI) = 0$ at that point, $f_{t/b} = \pm 2(t_x^q + t_y^q)$. If $t_y > t_x$, as $q \rightarrow \infty$, $\lambda_{\pm} \approx (2\tilde{f})^{\pm 1} \approx [2(t_y/t_x)^q \times ((-1)^{i_g} - \cos(k_y q))]^{\pm 1}$ (i_g denotes the number of bands that are below the gap) except when $((-1)^{i_g} - \cos(k_y q)) = 0$. In this case, the localization length of the edge state is given by $\xi = |q(\log |\lambda|)^{-1}| \approx \log(t_y/t_x)^{-1}$. A more careful analysis yields the next-order term, which is included in the main text. Thus in this case, except at some particular k_y , the edge state rapidly decays no matter how small the gap is. On the other hand, if $t_x > t_y$, as $q \rightarrow \infty$, $f \approx (-1)^{i_g} (1 + 2a_{p,q,i_g}^2 (E_g^2/4 - (e - E_{i_g,c})^2))$, where $E_{i_g,c}$ is the energy of the center of the i_g -th gap, and a_{p,q,i_g} is a positive constant. Therefore, at the center of the gap, $\lambda_{i_g,c,\pm} \approx (-1)^{i_g} (1 \pm \sqrt{4a_{p,q,i_g}^2 (E_g^2/4 - (e - E_{i_g,c})^2)}) = (-1)^{i_g} (1 \pm E_g a_{p,q,i_g})$, and $\xi \approx (a_{p,q,i_g} E_g)^{-1}$. In this case, the localization length of the edge state is inversely proportional to the gap. We also compared the numerically obtained w with the theoretically obtained w_T and found that as long as the gap is small enough (i.e. large Chern number) and q is large enough, the theoretic and numerical results coincides [Fig. S5(b,c)].

F. Finite temperature phase diagram in both directions

In this section, we also present the metal-insulator transition (MIT) in the x -direction and provide some details of the MIT in the y -direction. The MIT in the x -direction resembles that at $T = 0$, i.e. for sufficiently low temperatures, the system is insulating/metallic when the Fermi energy is in the gap/band [Fig. S6(c)]. This behavior indeed originates from the fact that the product of DOS and x -velocity is maximal at the center of the band [Fig. S6(d)]. For comparison, we also present a similar diagram in the y -direction.

In the main text, we also mention that the system is insulating in the y -direction for sufficiently large q and for almost all E_F , except in the immediate vicinity of the bulk-gap boundary. Specifically, for $q = 13$, the total range of such exceptional E_F is of the order of 10^{-3} , compared to the total energy range of 5.56.

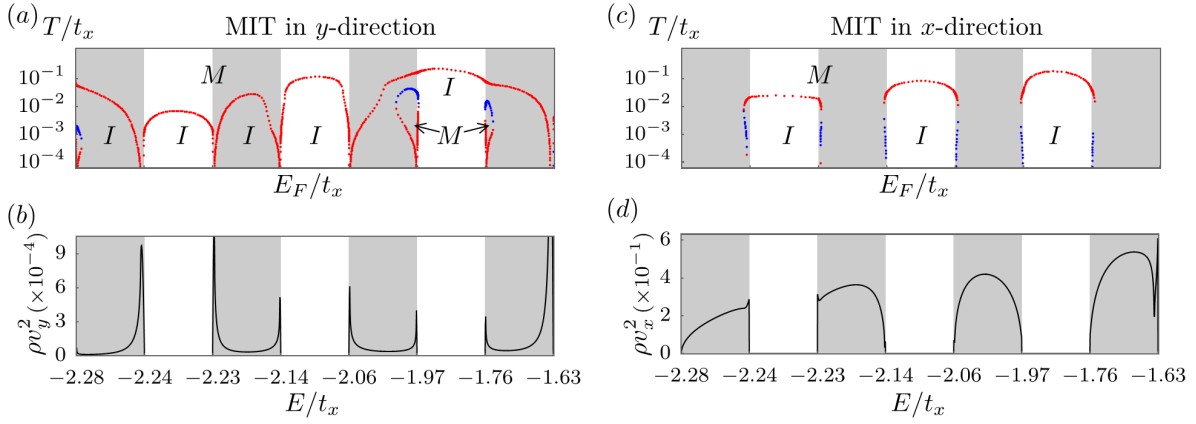


Figure S6. (a) The phase diagram classified by σ_{yy} . (b) The product of density of states (DOS) and y -velocity. (c) The phase diagram classified by σ_{xx} . (d) The product of DOS and x -velocity. Parameters chosen: $t_x = 1, t_y = 0.7, \Gamma = 1/100, \phi = 8/13$.

G. Characterization of the bulk state wavefunctions

Other quantities can also be used to characterize the localization and extension behavior of the wave function. We take periodic boundary conditions, choose the gauge $\mathbf{A} = 2\pi\phi j_y \hat{e}_x$, set $L_y = q$, and introduce a dimensionless quantity [S2]

$$\tilde{z} = \sum_{j_x j_y} e^{i2\pi j_y/q} |\psi_{j_x j_y}|^2. \quad (\text{S18})$$

In the extreme localized state (with $|\psi_{j_x j_y}|^2 \sim \delta_{j_x j_x 0, j_y j_y 0}$), $|\tilde{z}| \rightarrow 1$, and in the extreme extended state (with $|\psi_{j_x j_y}|^2 \sim (L_x L_y)^{-1}$), $|\tilde{z}| \rightarrow 0$. We numerically find that the quantity \tilde{z} is approximately independent of p and L_x , except for certain choices of p, q , and L_y where the system is highly degenerate, making \tilde{z} not well-defined since the eigenstates can be freely mixed within the degenerate subspaces. To avoid the numerical errors from high degeneracy, we define the mean of \tilde{z} as $z = \mathcal{N}^{-1} \sum_{p, L_x, m} |\tilde{z}|(p, L_x, m)$ to quantify the localization behavior of the whole system as a function of q , where \mathcal{N} is the total number of selected eigenstates (m is the eigenstate index) and the total number of selected samples with different p and L_x . The mean z is not affected by those p and L_x , for which the system is highly degenerate. For $q \rightarrow \infty$, we can see that $z \rightarrow 0$ for $t_x > t_y$, indicating the states along x direction to be extended, and $z \rightarrow 1$ for $t_x < t_y$, indicating the states along x direction to be localized [see Fig. S7(a)]. This is consistent with the results that we obtain using other quantities. On the other hand, one can see that $z \rightarrow \kappa \approx 0.52$ for $t_x = t_y$, which indicates that the system is neither localized nor extended, but critical. In comparison with the quantity z , the scaling of $\sigma_{yy}\Gamma$ in the limit $T = 0$ and small Γ regime can provide a clearer indicator of different regimes. For $t_y < t_x$, the conductance $\sigma_{yy}\Gamma$ decays exponentially with respect to q , implying localization in the y direction as $q \rightarrow \infty$, as shown in Fig. S7(b). For $t_y > t_x$, the conductance $\sigma_{yy}\Gamma$ is independent of q , implying metallic behavior in this direction. For $t_x = t_y$, the conductance exhibits a power-law decay with q , implying a critical regime.

As a comparison, we also plot $\langle C_2 \rangle$ and Δv [Fig. S7(c,d)], discussed in detail in part A, on a similar scale. For these two quantities, the critical point $t_x = t_y$ shows a power-law decay as a function of q , in contrast with an exponential decay as a function of q for the localized regime or the independence of q in the extended regime, indicating that, at the quasiperiodic limit, the bulk transport is qualitatively stronger than that in the localized regime, but qualitatively weaker than that in the extended regime, justifying that the system is indeed critical at the isotropic point $t_x = t_y$.

H. The isotropic case with $t_x = t_y$

In this section, we further establish the essential differences between the isotropic case $t_x = t_y$ and the anisotropic case by investigating the conductivity σ_{yy} at $T = 0$ with finite relaxation rate Γ , which reveals intriguing effects. We begin by focusing on the aforementioned asymptotic behavior ($T = 0$, small Γ) of the conductivity, i.e., σ_{yy} decays exponentially, decays algebraically or remains unchanged as q increases at $t_x > t_y$, $t_x = t_y$, or $t_y > t_x$, respectively. This behavior can be inspected both in Fig. S7(b) and Figs. S8(a-c). As shown in Figs. S8(a,b), the gray tilted arrows indicate the direction of increasing q , which is set to be $q = 13, 21, 34, 55$ and 89 . In the anisotropic regime with $t_x > t_y$ [Fig. S8(a)], the spacing between the straight lines in the Metal II region increases exponentially, indicating an exponential scaling of conductivity versus q . In contrast, at

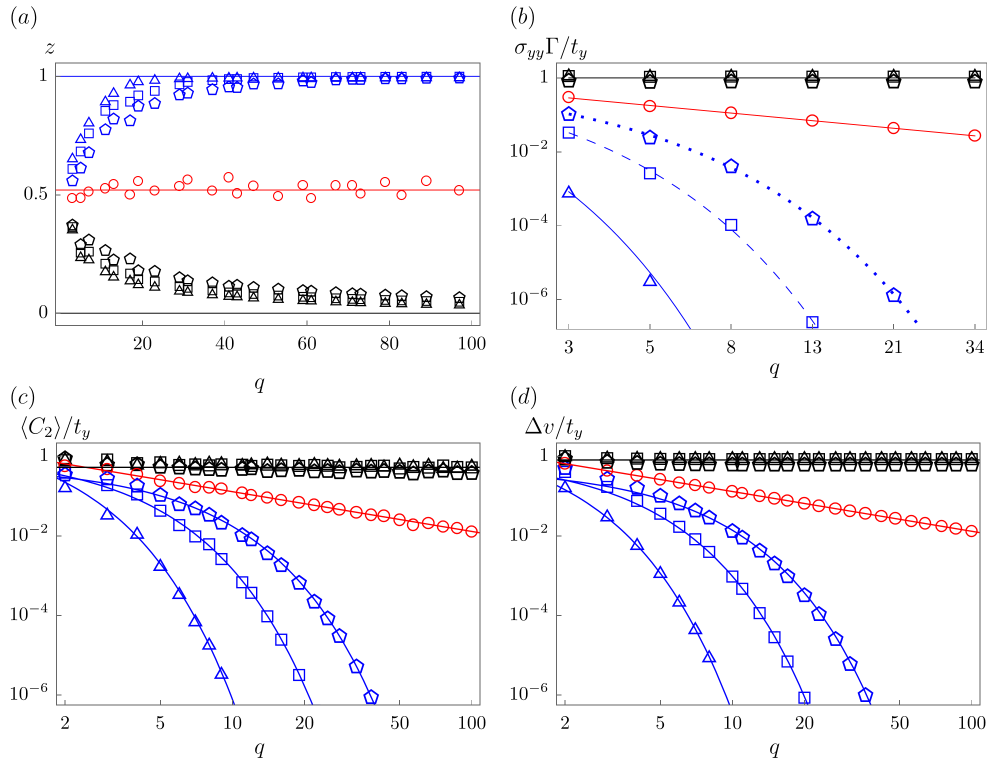


Figure S7. In all subgraphs, $t_x = 1$. The black pentagon, square and triangle represent $t_y = 4$, $t_y = 3$ and $t_y = 2$, respectively. The red circle represents $t_y = 1$. The blue pentagon, square and triangle represent $t_y = 0.7$, $t_y = 0.5$ and $t_y = 0.2$, respectively. The black, red, blue lines indicate asymptotic behavior or fitted scaling in the extended, critical and localized regimes, respectively. (a) z vs q : $z \rightarrow 1$ in the localized regime (blue line) and $z \rightarrow 0$ in the extended regime (black line). In the critical regime, $z \rightarrow \kappa \approx 0.52$ as indicated by the red line. (b) The conductivity $\sigma_{yy}\Gamma/t_y$ vs q . (c) $\langle C_2 \rangle/t_y$ vs q . (d) Δv vs q . (b-d) In the localized regime, the blue fitted line indicates an exponentially decaying tendency as q increases, while the red fitted line indicates an algebraically decaying tendency. The black fitted line indicates independence of q .

the isotropic regime with $t_x = t_y$ [Fig. S8(b)], the lines are equally spaced, indicating a power-law scaling of conductivity versus q in this region. Lines in Fig. S8(c) overlap, indicating that the conductivity is independent of q . Beyond the small Γ limit, we found that the critical relaxation rate Γ_{c2} , which denotes the leftmost phase boundary in Fig. S8(a) and Fig. S8(b), decreases exponentially and algebraically, respectively. Most nontrivially, in the middle region with $\Gamma_{c2} < \Gamma < \Gamma_{c1}$, the original insulator for $t_x > t_y$ turns into a critical metal (Metal III) at the isotropic point $t_x = t_y$ under the interplay between asymptotic quasiperiodicity and relaxation. In the critical metal phase, the conductivity satisfies $\sigma \sim \Gamma^{-0.5}$, which is a unique behavior not seen in the localized or extended phases. Similar to the above discussion, these results suggest that at the isotropic point $t_x = t_y$, the system is deeply connected to the critical phase in the quasiperiodic limit. For comparison, we also plot a graph simultaneously showing the three cases ($t_x > t_y$, $t_x = t_y$ and $t_x < t_y$) together [Fig. S8(d)].

[S1] J. Sokoloff, Unusual band structure, wave functions and electrical conductance in crystals with incommensurate periodic potentials, *Physics Reports* **126**, 189 (1985).

[S2] R. Resta and S. Sorella, Electron localization in the insulating state, *Phys. Rev. Lett.* **82**, 370 (1999).

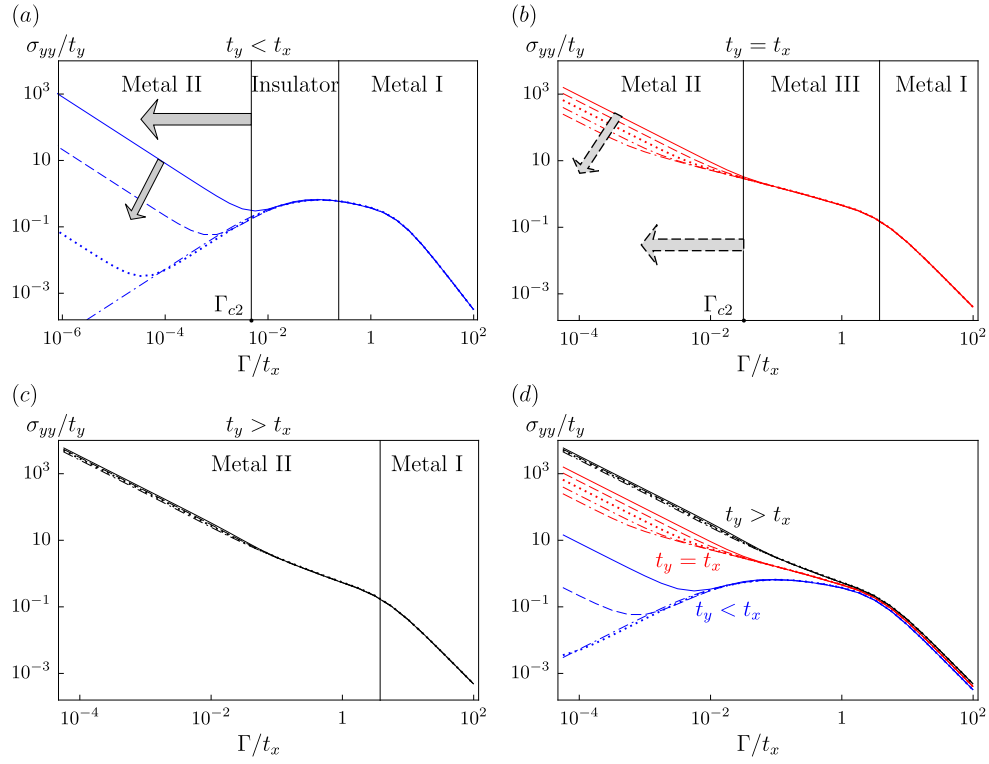


Figure S8. σ_{yy} vs Γ , where $t_x = 1$ and $t_y = 1.2$ (a); $t_y = 1$ (b) or $t_y = 0.8$ (c), respectively. $\phi = 8/13, 13/21, 21/34, 34/55$ and $55/89$, corresponding to the solid, dashed, dotted, dashed-dotted and dashed-dashed-dotted lines, respectively. Blue, red and black colors correspond to three different parameter conditions $t_x > t_y$, $t_x = t_y$ and $t_x < t_y$, respectively. Gray arrows indicate the behavior as q increases. Two metallic regions (Metal I/II) with distinct origins are shown in (a,b,c). The middle region denotes an insulator phase in y direction for $t_x < t_y$ (a), and a critical metal phase for $t_x = t_y$ (b). E_F is set within a band. (d) The combined plot of (a-c) for a comparison.